



Methane emissions from a Californian landfill, determined from airborne remote sensing and in-situ measurements

Sven Krautwurst¹, Konstantin Gerilowski¹, Hafliði H. Jonsson², David R. Thompson³, Richard W. Kolyer⁴, Andrew K. Thorpe³, Markus Horstjann¹, Michael Eastwood³, Ira Leifer⁵, Sam Vigil⁶, Thomas Krings¹, Jakob Borchardt¹, Michael Buchwitz¹, Matthew M. Fladeland⁴, John P. Burrows¹, and Heinrich Bovensmann¹

¹Institute of Environmental Physics (IUP), University of Bremen, Bremen, Germany

²Center for Interdisciplinary Remotely-Piloted Aircraft Studies (CIRPAS), Marina, CA, US

³Jet Propulsion Laboratory (JPL), California Institute of Technology (Caltech), Pasadena, CA, US

⁴Earth Science Division, NASA Ames Research Center (ARC), Mountain View, CA, US

⁵Bubbleology Research International (BRI), Goleta, CA, US

⁶California Polytechnic State University (CalPoly), San Luis Obispo, CA, US

Correspondence to: Sven Krautwurst (krautwurst@iup.physik.uni-bremen.de)

Abstract. Fugitive emissions from waste disposal sites are important anthropogenic sources of the greenhouse gas methane (CH₄). As a result of the growing world population and the recognition of the need to control greenhouse gas emissions, this anthropogenic source of CH₄ has received much recent attention. However, the accurate assessment of the CH₄ emissions from landfills by modeling and existing measurement techniques is challenging. This is because of inaccurate knowledge of the model parameters and the extent of and limited accessibility to landfill sites. This results in a large uncertainty in our knowledge of the emissions of CH₄ from landfills and waste management.

In this study, we present results derived from data collected during the research campaign COMEX (CO₂ and Methane EXperiment) in late summer 2014 in the Los Angeles (LA) Basin. The objective of COMEX, which comprised aircraft observations of methane by the remote sensing Methane Airborne MAPper (MAMAP) instrument and a Picarro greenhouse gas in-situ analyser, was the quantitative investigation of CH₄ emissions.

Enhanced CH₄ concentrations or „CH₄ plumes“ were detected downwind of landfills by remote sensing aircraft surveys. Subsequent to each remote sensing survey, the detected plume was sampled within the atmospheric boundary layer by in-situ measurements of atmospheric parameters such as wind information and dry gas mixing ratios of CH₄ and carbon dioxide (CO₂) from the same aircraft. This was undertaken to facilitate the independent estimation of the surface fluxes for the validation of the remote sensing estimates.

During the COMEX campaign, four landfills in the LA Basin were surveyed. One landfill has repeatedly shown a clear emission plume. This landfill, the Olinda Alpha Landfill, was observed on four days during the last week of August and first days of September 2014. Emissions were estimated for all days using a mass balance approach. The derived emissions are between 13.0 and 18.2 kt CH₄ yr⁻¹ with related uncertainties in the range of 17 % to 46 %. The comparison of the remote sensing and in-situ based CH₄ emission rate estimates reveals good agreement within the error bars with an average absolute difference of around 2.3 kt CH₄ yr⁻¹. The US Environmental Protection Agency (EPA) reported inventory value is 11.5 kt CH₄ yr⁻¹ in



2014, on average $3.0 \text{ kt CH}_4 \text{ yr}^{-1}$ ($\pm 1.5 \text{ kt CH}_4 \text{ yr}^{-1}$) lower than our estimates acquired in late Summer 2014. This difference may in part be explained by a possible leak located on the south-western slope of the landfill, which we identified in the observations of the Airborne Visible / Infrared Imaging Spectrometer - Next Generation (AVIRIS-NG) instrument, flown contemporaneously aboard a second aircraft on one day.

5 1 Introduction

Methane (CH_4) is one of the most important anthropogenic greenhouse gases modulated by human activity. According to Kirschke et al. (2013), the methane emissions from landfills and waste management contribute around 20% to 27%¹ of the global anthropogenic methane emissions budget. Under anaerobic conditions, bacteria produce CH_4 by consuming biodegradable waste, which has been deposited within the landfill. This is known as landfill gas (LFG), which contains CH_4 as its major component (typically between 50% to 60%), carbon dioxide (CO_2) and other gases (e.g., Eklund et al., 1998; Amini et al., 2012).

Modern landfills (NSWMA, 2006) are often covered with special oxidation layers and also equipped with tubes embedded vertically and / or horizontally within the landfill, through which the LFG is collected. The collected LFG is often used (and converted to CO_2) in small dedicated power plants for electricity and heat generation and, thus, reduces the environmental impact of the landfill emissions. When not used for power generation, collected LFG is sometimes flared, which also oxidises CH_4 to CO_2 having a lower global warming potential (Myhre et al., 2013).

Nevertheless, not all of the CH_4 is captured by the LFG collection system and subsequently converted to CO_2 . The amount of the remaining CH_4 escaping into the atmosphere depends on the engineering approaches used to manage the landfill and atmospheric boundary layer conditions. For instance, the type and material of the landfill cover can decrease (Trapani et al., 2013) or increase emissions (Capaccioni et al., 2011). Trapani et al. (2013) have also found that slopes of landfills are areas with an enhanced CH_4 release. Additionally, atmospheric pressure variations (Czepiel et al., 2003; Poulsen et al., 2003; Gebert and Groengroeft, 2006; Trapani et al., 2013; Xu et al., 2014) or surface wind speeds (Poulsen and Moldrup, 2006) can modulate CH_4 emissions into the atmosphere.

Both measurements of CH_4 and models of the processes producing CH_4 in landfill sites can be used to estimate their emissions. Commonly used for reporting and recommended by IPCC (2006) are first-order decay (FOD) waste models. They are based on knowledge of the amount of available degradable waste, which is consumed by the bacteria, how it decays over time, but also consider other parameters such as the type and age of the waste, its temperature, moisture content and oxidation capacity of the landfill cover (Amini et al., 2013). Studies comparing direct measurements to model estimates have found that the modeled outputs can significantly differ from actual measurements (Amini et al., 2012, 2013).

However, measurements are also challenging because landfills typically have a relatively large surface area, an irregular topography and the emissions are not distributed homogeneously across the landfill. Babilotte et al. (2010) compared five different techniques measuring emissions from the same landfill. The study included ground based in-situ (tracer gas method,

¹<http://www.globalcarbonproject.org/methanebudget/>, last access: 29.09.2016



inverse modeling of direct CH_4 measurements), ground based remote sensing (laser plume mapping, differential absorption light detection and ranging), and an airborne based method (helicopter-borne infrared laser spectroscopy at around $1.65\ \mu\text{m}$). The CH_4 emission rate estimates of the landfill under consideration and of a controlled release experiment performed in that study disagreed by a factor of 5 to 10.

- 5 Several other studies used airborne based in-situ measurements to characterize the total emissions of landfills (e.g., Peischl et al., 2013; Lavoie et al., 2015, and references therein). In these studies different flight strategies and mass balance approaches were used. Emission uncertainties are typically estimated to be between approximately 20 % and 30 %. However, airborne in-situ measurements are often restricted by Air Traffic Control (ATC) regulations such as minimum safe altitude and ATC control zones.
- 10 Recently, airborne thermal-infrared (TIR, 7.5 to $13.5\ \mu\text{m}$) imaging spectrometry measurements have been tested to locate CH_4 emissions also from landfills (Tratt et al., 2014). The study succeeded to derive emission rates for two localized on-site emitters - a compressed natural gas (CNG) fueling station and a gas-flaring station - with relative errors of 50 % and 120 %. However, integrated emissions for the entire landfill were not reported.

In this manuscript, we present a data set collected by two different techniques i.e. passive airborne remote sensing and
 15 airborne in-situ cavity ring down spectroscopy (CRDS). They were used to independently estimate the emission rate of a particular landfill in the Los Angeles (LA) Basin on four different days in late summer 2014. The passive airborne remote sensing method is based on medium spectral resolution ($\sim 0.9\ \text{nm}$) solar absorption spectroscopy in the short wave infrared (SWIR) region around $1.65\ \mu\text{m}$. To assess the total CH_4 landfill emissions, a mass balance approach is used. The emission estimates, derived by this method, are compared to emission estimates calculated using airborne in-situ measurements acquired
 20 from the same aircraft. Emissions are estimated using a Kriging method for interpolation of the data in combination with a mass balance approach (in a similar way as described in, e.g., Lavoie et al., 2015, and references therein). In addition, imaging spectroscopy observations from another passive remote sensing instrument installed aboard of a second aircraft were utilized to identify emission hotspots across the landfill by analysing measured spectra in the region around $2.3\ \mu\text{m}$ at low spectral resolution ($\sim 5\ \text{nm}$).

- 25 This article is structured as follows: After describing the research campaign in which the flights were embedded, the selected target is introduced in Sect. 2. In Sect. 3, the participating instruments and collected data sets are summarized. In Sect. 4, the flight strategy is presented. The retrieval methods are described in Sect. 5. In Sect. 6, the emission rate results, their errors and the retrieval results from the imaging instrument aboard the second aircraft are reported. A comparison of the results from the different instruments is presented in Sect. 7. The manuscript closes with a summary and conclusions (Sect. 8).

30 2 Campaign and target description

The measurement flights presented in this work were part of the CO_2 and Methane EXperiment (COMEX), which was conducted in the San Joaquin Valley (SJV) and greater Los Angeles in May/June and August/September 2014. COMEX was a collaborative effort between the National Aeronautics and Space Administration (NASA) and the European Space Agency (ESA),

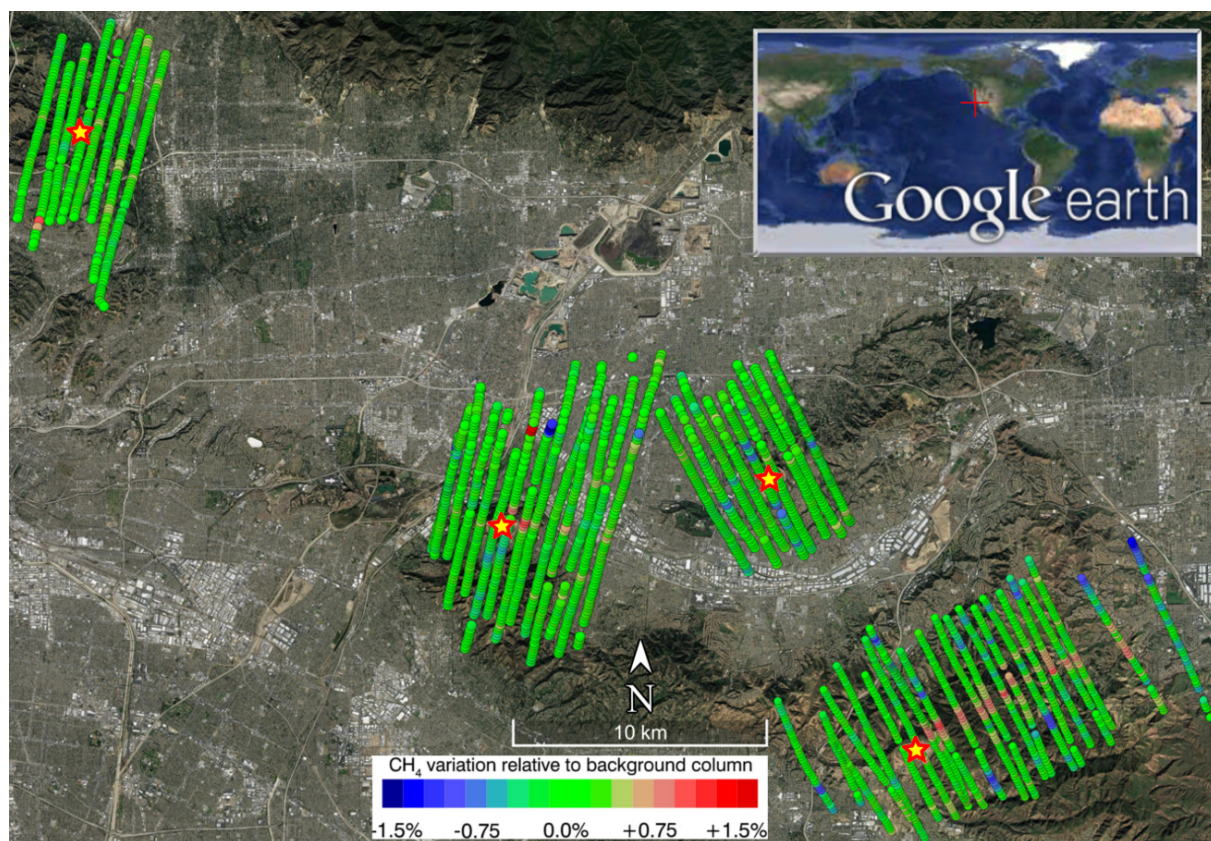


Figure 1. Shown are the MAMAP remote sensing survey flights over the four landfills (from left to right: the Scholl Canyon Landfill on 27.08.2014, the Puente Hills Landfill on 27.08.2017, the BKK Corporation Landfill on 01.09.2014 and the Olinda Alpha Landfill on 01.09.2014) in the Los Angeles Basin (red cross in the world map, top right) in the main overview plot. Their locations are marked by red/yellow stars. The MAMAP measurements are filtered by inclination to remove the turns and the colour code depicts CH_4 variations relative to the background (for details, see Sect. 5.1). Only the Olinda Alpha Landfill shows a clear plume in downwind direction. The wind direction was in general from south-west during the measurements. The map underneath is provided by Google Earth.

in support of the development of the two satellite concept missions HypsIRI (Lee et al., 2015) and CarbonSat (Bovensmann et al., 2010; Buchwitz et al., 2013; ESA, 2015). The main focus of the campaign addressed the assessment of anthropogenic CH_4 emissions. In addition to measurements over and in the plumes of landfills, flights were made to determine emissions from oil fields (Thompson et al., 2015; Gerilowski et al., 2014), offshore seep fields and animal husbandry.

- 5 In total four different landfills were surveyed in the greater LA area: the Scholl Canyon Landfill, the Puente Hills Landfill, the BKK Corporation Landfill and the Olinda Alpha Landfill. Only the latter showed continuously detectable and well-developed plume structures during the remote sensing surveys (Fig. 1).

In this manuscript, we therefore focus on the datasets collected over the Olinda Alpha Municipal Landfill. All measurements showed a pronounced CH_4 plume over the investigated time period. The landfill is located in Orange County, Los Angeles



Basin, CA, USA (at 33.939° N, 117.836° W; Fig. 2). Measurements were acquired on four different days in the middle of the afternoon, during the last week of August and the first days of September 2014. On flight days, skies were clear and winds were from south-west to west at around 4 to 8 m s⁻¹.

The Olinda Alpha Landfill started operation in 1960 and is expected to close by 2030. It accepts a maximum of 8,000 tons of municipal solid waste daily and occupies an area of around 2.3 km². Since 2012, a 32.5 MW combined cycle power plant has been using the LFG to generate electricity for around 22,000 homes². According to the US Environmental Protection Agency³ (EPA), the estimated CH₄ amount released into the atmosphere was 11.5 kt CH₄ in 2014 dropping from a peak value of 15.4 kt CH₄ in 2011 to 14.3 kt CH₄ in 2013.

3 Aircraft instrumentation and collected data sets

All instruments used for a quantitative analysis were flown aboard a DHC-6 Twin Otter (TO) aircraft operated by the Center for Interdisciplinary Remotely-Piloted Aircraft Studies (CIRPAS⁴). These comprise: the Methane Airborne MAPper (MAMAP), a Picarro CDRS greenhouse gas in-situ analyser, and the CIRPAS aircraft standard research instrumentation suite including different positioning and attitude, meteorological, aerosol, cloud and precipitation sensors.

The remote sensing instrument MAMAP (Gerilowski et al., 2011) was developed by the Institute of Environmental Physics (IUP), University of Bremen, in cooperation with the German Research Centre for Geoscience (GFZ) in Potsdam. It measures reflected and scattered solar radiation from the surface in the spectral region between 1.59 and 1.69 µm at medium spectral resolution of around 0.9 nm to retrieve total column concentration information of CH₄ and CO₂. For the current flights, a fibre coupled entrance telescope (connecting the telescope via a 5 m glass fibre bundle to the spectrometer) was installed on a gyro stabilized platform (SOMAG, type: CSM-130⁵) to ensure nadir viewing geometry. The column information derived from MAMAP is used in combination with knowledge of the wind fields for the calculation of emission rates.

The Picarro fast greenhouse gas in-situ analyser (type: G-2301f) was provided by the NASA's Ames Research Center (ARC) and operated by IUP during the flights. The instrument uses the CRDS technique (Crosson, 2008) to measure CH₄, CO₂ and water vapour (H₂O) in-situ concentrations at flight altitude at a frequency of around 1.7 Hz. The air samples entered the aircraft through an atmospheric in-situ sampling boom and then were transported via a PTFE tubing system to the measurement cavity of the CRDS instrument. This process induces a time delay (in the following referred to as time lag) between the position where the air samples are acquired in the atmosphere and the time of measurement in the ring down cavity of the instrument onboard the aircraft. This time lag was estimated from measurements in the laboratory to be around 21 s with an associated uncertainty conservatively estimated to be ± 5 s. Dry gas mixing ratios of CH₄ and CO₂ were calculated by the software of the analyser via the synchronously measured water vapour (Rella, 2010). These measurements are used for an independent in-situ

²<http://oclandfills.com/landfill/active/olindalandfill>, last access: 21.06.2016

³<https://ghgdata.epa.gov/ghgp/service/facilityDetail/2014?id=1002320&ds=E&et=undefined&popup=true>, last access: 07.07.2016

⁴<http://www.cirpas.org/>, last access: 17.10.2017

⁵<http://www.somag-ag.de/csm-130/>, last access: 02.08.2016



based emission estimate. This enables a comparison to be made with the emission estimated by the MAMAP remote sensing data.

The CIRPAS aircraft standard research instrumentation suite delivers auxiliary data. These comprise, for example, 3D position information (attitude heading), wind information (speed and direction derived from a 5-hole turbulence probe), and information for the characterization of the atmosphere (e.g., potential temperature, aerosol load, ambient temperature, pressure) at a frequency of 10 or 1 Hz depending on the measured parameter.

On one flight day, the CIRPAS TO was accompanied by a second Twin Otter aircraft flying the Airborne Visible / Infrared Imaging Spectrometer - Next Generation (AVIRIS-NG - Hamlin et al., 2011; Green et al., 1998) operated by the Jet Propulsion Laboratory (JPL). AVIRIS-NG also measures backscattered solar radiation from the surface to infer column information on CH_4 . In contrast to MAMAP, AVIRIS-NG is an imaging instrument with a high spatial sampling but relatively low spectral resolution of 5 nm and a wide spectral range from 0.38 to 2.51 μm . Typical CH_4 retrievals use the spectral region from 2.1 to 2.4 μm . In this study, we use the AVIRIS-NG instrument's imaging capabilities to identify potential source position(s) of CH_4 emitted by the landfill, which was not possible with the non-imaging MAMAP instrument (Thompson et al., 2015).

4 Flight strategy

To achieve the goal of estimating the emission rate of an areal source like a landfill (here: around 2.3 km^2) using combined aircraft remote sensing and in-situ observations by the MAMAP and Picarro instruments, an appropriate flight pattern needs to be flown by the aircraft. The measurements during the flights were divided into two parts: 1) remote sensing measurements of the CH_4 plume from above the atmospheric boundary layer covering the entire area by a dense pattern and 2) in-situ measurements intersecting the entire plume within the atmospheric boundary layer.

The remote sensing and in-situ flight patterns implemented during the campaign were developed and optimized during pre-flight planning on the basis of the above requirements as well as taking into account the weather forecast, restrictions due to Air Traffic Control (ATC), and available flight time. Each acquisition started with remote sensing measurements and was followed by in-situ measurements.

Performing the remote sensing measurements first has a significant advantage as a CH_4 real-time retrieval utilizing the MAMAP data has been implemented for the COMEX campaign. If the real wind direction deviates from the forecast, this approach allows the operator to dynamically adjust the flight pattern accordingly to match the plume location obtained from the remote sensing total column information. The latter is dynamically superimposed on Google Earth map data.

The remote sensing tracks are flown typically above the atmospheric boundary layer in a dense pattern perpendicular to the wind direction covering the entire measurement area. In-situ CH_4 and CO_2 data were also acquired during these measurements providing information on CH_4 and CO_2 concentration distributions in the measurement area above the boundary layer.

To ensure a good coverage of the vertical extent of the plume during the second part of the flight focusing on in-situ measurements, the aircraft typically flew at a fixed distance from the source for several plume transects perpendicular to the prevailing wind direction at different altitudes trying to best cover the entire boundary layer. The number of legs for such a

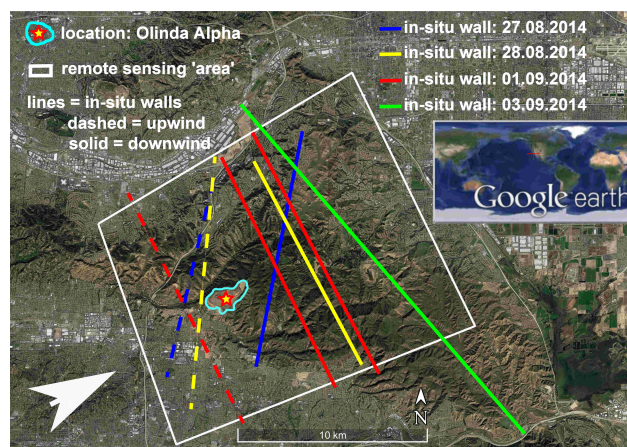


Figure 2. The Olinda Alpha Landfill is located at the position of the red/yellow star encircled by the cyan solid line. Additionally, the approximate positions of the flown in-situ upwind (dashed lines) and downwind (solid lines) walls (see Sect. 4 for details) and the area which were surveyed by the MAMAP remote sensing instrument (white box) are shown. The colours of the in-situ walls represent the different flight days at the Olinda Alpha Landfill: Blue: 27.08.2014. Yellow: 28.08.2014. Red: 01.09.2014. Green: 03.09.2014. The white arrow indicates the approximate prevailing wind direction for measurement flights over the Olinda Alpha Landfill. The map underneath is provided by Google Earth.

“wall” of measurements varies depending on the available flight time, between 3 and 6. Additionally, depending on available flight time such a wall was typically flown upwind and downwind characterizing the inflow and outflow to the area. On one day, one additional downwind wall of measurements was located at a distance further away from the source to better characterize occurrent errors on the estimated fluxes. The maximum altitude extent of the plume is generally well documented, as on all four flight days, there is at least one leg, which shows no plume structures or signals and therefore confines the upper limit of the plume. Due to ATC restrictions over congested areas like the Los Angeles Basin, flying below 1000 ft above ground level (ft agl, equals around 300 m agl) was not permitted. Therefore, the lowest measured track was typically extrapolated down to the surface following the terrain (more details are given in Sect. 6.2). Figure 2 shows the approximate position of the three upwind (dashed lines) and five downwind (solid lines) walls flown on all four days.

The flight pattern performed by the second aircraft with the imaging AVIRIS-NG instrument aboard was different. Due to its relatively wide swath, it needed only one flight line to cover the entire landfill. Measurements were acquired while flying well above the boundary layer approximately parallel to the prevailing wind direction.

5 Retrieval algorithms and calculation of emission rates

The following sections present the steps necessary to obtain the emission rates from the measurements collected by the different instruments. Section 5.1 describes the MAMAP retrieval algorithm and the assessment of the emission rate estimates. Section



5.2 explains how the in-situ data collected by the Picarro instrument is used to determine emission rate estimates. In addition, the retrieval of the CH₄ anomaly maps from the AVIRIS-NG imaging data is described in Sect. 5.3.

5.1 MAMAP retrieval algorithm and emission rate estimates

In order to retrieve the column amounts of CH₄ and CO₂ from the measured spectra, we used the Weighting Function Modified Differential Optical Absorption Spectroscopy (WFM-DOAS) method (for details, see Buchwitz et al., 2000; Krings et al., 2011, 2013). In general, the algorithm minimizes the differences between the logarithm of the measured spectra and a spectrum computed by a linearised Radiative Transfer Model (RTM), which describes the general or mean state of the atmosphere during the flight. The differences between the modelled and measured parameters are minimized by varying selected parameters or fit factors on, e.g., the methane profile and atmospheric parameters. The CH₄ in the plume from landfill emissions is seen to be enhanced relative to the surrounding air.

The WFM-DOAS algorithm has successfully been applied to aircraft MAMAP measurements and used to investigate the emissions of point sources at known locations having flue gas or ventilation stacks / chimneys with diameters of below 50 m, such as those from CO₂ emitting power plants (Krings et al., 2011, 2016) and CH₄ emitting ventilation shafts of coal mines (Krings et al., 2013). In contrast to the previous studies, we apply the approach to an areal source i.e. a landfill (with a size of around 2.3 km²), where the exact locations of the emission(s) are not known but limited by the approximate area of the landfill. As a result of the larger area of this source and the resulting wider plume, the expected column enhancements within the plume are typically lower in comparison to enhancements produced by point sources with diameters smaller than 50 m having the same source magnitude for similar atmospheric conditions.

For each flight a dedicated set of RTM computations were calculated to account for the varying atmospheric conditions on the different days. Additionally, a change in the solar zenith angle (SZA) and surface elevation along the flight track are taken into account by performing RTM simulations to generate a 2-dimensional look-up table, which is then used in the retrieval. The surface elevation is based on data from the Shuttle Radar Topography Mission (SRTM) digital elevation model version 2.1⁶ which has a spatial resolution of one arc second (around 30 m at the equator) in the U.S.A. Additionally, the remaining parameters flight altitude, surface albedo and atmospheric background profiles were also adapted to the current flight conditions:

- The surface is assumed to have a Lambertian reflectance and for the spectral band of CH₄ and CO₂ to have no spectral dependency. The surface spectral reflectance or albedo values used are taken from Chen et al. (2006). They use clear-sky radiances measured by the Moderate Resolution Imaging Spectrometer (MODIS) onboard the Terra satellite and the Visible Infrared Scanner (VIRS) onboard the Tropical Rainfall Measuring Mission (TRMM) spacecraft to retrieve the surface albedo in different spectral channels for different surface type categories defined by the International Geosphere Biosphere Programme (IGBP). As the MAMAP instrument operates in the SWIR region around 1.65 μm, we use the surface albedo derived from the 1.6 μm channel of MODIS and VIRS. Assuming that the surface type at and around

⁶http://dds.cr.usgs.gov/srtm/version2_1/, last access: 15.06.2016



the landfill can be described as a composite of approximately 50 % 'urban' and 50 % 'open shrubland' (corresponding to a retrieved surface spectral reflectance or surface albedo of around 0.22 and 0.40 (Chen et al., 2006, their Table 1), respectively), this yields a mean surface albedo of 0.31.

- For the background profiles of CH₄ and CO₂, which describe the mean background concentrations of these gases in the measurement area (and are not influenced by, for example, the landfill emissions) the vertical profiles from the U.S. standard atmosphere were used and adapted to current concentrations by using data collected by the Picarro greenhouse gas in-situ analyser. The profiles of CH₄ and CO₂ in the lower part of the troposphere were replaced by a polynomial fitted to the measured profile corresponding to the first descent from remote sensing altitude to the lowest possible in-situ flight leg. In-situ measurements gathered at remote sensing altitude are assumed to belong to the free troposphere and, thus, were used to scale the entire upper part of the U.S. standard profiles.

The HITRAN 2012 spectroscopic database for line parameters (Rothman et al., 2013) and a standard OPAC (Optical Properties of Aerosols and Clouds) urban aerosol scenario (Krings et al., 2011, 2013, 2016) were used in the RTM calculations, as the landfill is located within Los Angeles Basin.

The column-averaged dry air mole fractions XCH₄, which are later used in the estimation of the CH₄ emission rate, were retrieved utilising the XCH₄(CO₂) proxy method. This assumes a spatially and temporally constant CO₂ background concentration in the measurement area during the time remote sensing measurements are taken. In contrast to Krings et al. (2013), where coal mine ventilation shafts emitted only CH₄ and no significant amounts of CO₂, this assumption is violated for the Olinda Alpha Landfill. For landfills, it is expected that the co-emitted CO₂ may have an influence on the obtained XCH₄(CO₂) (or short XCH₄) columns when this proxy method is used. The impact is further investigated in Sect. 6.1.1.

The procedure to estimate the CH₄ emissions from the retrieved MAMAP XCH₄ data comprises the following steps. The data is first filtered by a signal filter to remove spectra with very low signal (less than 3000 counts) or spectra in saturation (as in Krings et al., 2011). Additionally, an inclination filter of ±5° is applied to eliminate measurements during aircraft turns or insufficient gyro stabilization by the CSM-130. Furthermore, the data obtained for each flight track is normalised by data obtained at its edges / flanks outside the plume (Krings et al., 2016). This step is necessary to remove a possible constant offset from the data (see also Krings et al., 2011) and to account for potential horizontal CH₄ or CO₂ concentration gradients.

Based on these measured column-averaged dry air mole fractions, XCH₄ (or CH₄ variations relative to the background column), a flux corresponding to each track is estimated by applying a mass balance approach (similar to that used in Krings et al., 2011, 2013, 2016):

$$F_{\text{RS}} = f_{\text{RS}} \cdot \frac{1}{n} \sum_i^n u_{\text{perp},i} \sum_j^{k_i} V_{i,j} \cdot \Delta x_{i,j} \quad (1)$$

where n is the total number of flight tracks downwind of the landfill flown on a certain day, k_i is number of measurements of a certain flight track i , V is the retrieved CH₄ variation relative to the background column in molec m⁻² of measurement j for track number i , $\Delta x_{i,j}$ is the length segment in m of a certain measurement j of track number i , $u_{\text{perp},i}$ is the wind speed



component perpendicular to the flight track i in m s^{-1} , f_{RS} is a conversion factor including the mass per CH_4 molecule and the time conversion from s to yr ($8.398 \cdot 10^{-25} \text{ kt s molec}^{-1}$) in order to calculate the emission rate F_{RS} in $\text{kt CH}_4 \text{ yr}^{-1}$ based on the MAMAP remote sensing measurements. The emission rate is given in $\text{kt CH}_4 \text{ yr}^{-1}$ but is strictly speaking only valid for the time of the overflight.

- 5 As in previous studies, the required wind direction is directly estimated from the measurements (observed plumes) themselves. The wind speed is provided by the 5-hole turbulence probe of the CIRPAS instrumentation, whereas only wind measurements collected in the area of the plume are used. Further details of the definition of the plume area for the wind estimates are given in Sect. 6.2.

5.2 In-situ emission rate estimates by Picarro data

- 10 Fluxes from the Picarro data were estimated separately for each downwind wall by the procedure described below. An in-situ wall of measurements comprises several flight legs flown at different altitudes. Usually these flight legs are not aligned perfectly parallel to each other and separated by around 150 m in altitude. For interpretation and estimation of reliable emission rates, the in-situ measurements were projected on a well-defined plane and perpendicular surface and the gaps between different tracks were filled by inter- and extrapolating, respectively, the measurements to a regular 2D grid on that plane.
- 15 Before the measurements from the flight legs of each wall were projected onto the plane surface, which is called the in-situ wall in the following, they were first corrected for the time lag of 21 s resulting from the tubing system (Sect. 3). The approximate positions of those in-situ walls are drawn in Fig. 2. The projection of the CH_4 measurements is shown in Fig. 4 (a) for the first downwind wall on the 01.09.2014. Figure 4 further comprises (b) the interpolated CH_4 mixing ratios, (c) the background CH_4 mixing ratios and (d) the enhanced CH_4 mixing ratios attributed to the plume of the landfill resulting from
- 20 the next processing steps described in the following.

- For the inter- and extrapolation, the statistical Kriging method (Kriging, 1951) was chosen. A similar approach has also been used in, e.g., Mays et al. (2009), Cambaliza et al. (2014) and Lavoie et al. (2015), to determine the outflow of cities and emissions of landfills. It is used to estimate values at locations, where no sample had been measured (in our case, mostly between the projected flight legs), with the aid of statistical methods. This method is described by the three parameters nugget, sill and range, which describe the statistics of the data set. The nugget stands for the small scale variability, the sill is the variance and the range gives the distance at which the samples are not correlated any more.

All three parameters can be inferred from an experimental semivariogram (Fig. 3) calculated by the following equation (e.g., after Isaaks and Srivastava, 1989; Cressie, 1993; Caers, 2011):

$$y(h_j) = \frac{1}{2N(h_j)} \sum_{N(h_j)} [V(s_i) - V(s_i + h_j)]^2 \quad (2)$$

- 30 where h_j 's are equidistant lag distances (e.g., ... 120 m, 160 m, 200 m, ...) which are separated by a constant lag separation distance h_{sep} (e.g., 40 m). The lag distance h_j describes the distance of the position between two measurements for which the semivariogram value $y(h_j)$ is calculated (Fig. 3, black crosses), whereby $N(h_j)$ is the number of data pairs for the respective lag distance h_j and the sum denotes the summation over all data pairs i which are separated by a certain lag distance h_j . $V(s_i)$

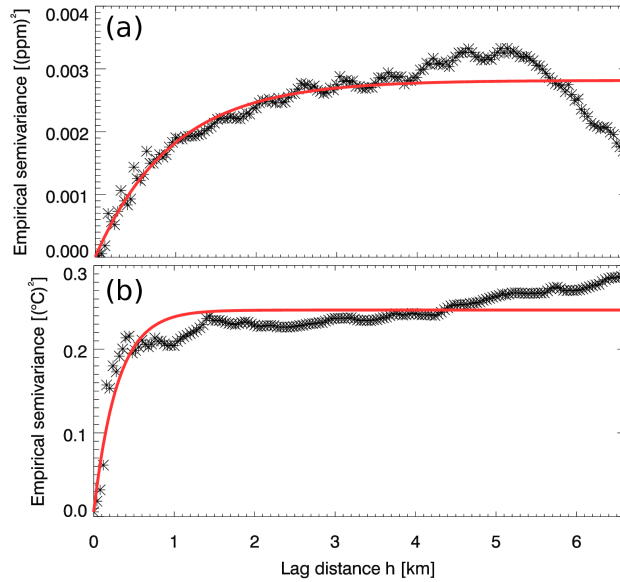


Figure 3. Example experimental semivariograms of (a) the in-situ dry gas mixing ratio of CH₄ and (b) the ambient temperature for the second downwind wall of the Olinda Alpha Landfill measurements on 01.09.2014. The black crosses depict the values of the empirical semivariance at certain lag distances h_j and the solid red line is the fitted exponential function. The fitted parameters of the exponential model are: Range: (a) 2.9 km, (b) 0.9 km; partial sill: (a) $2.8 \cdot 10^{-3} \text{ ppm}^2$, (b) $2.4 \cdot 10^{-1} \text{ °C}^2$; nugget: (a) $4.9 \cdot 10^{-6} \text{ ppm}^2$, (b) $5.7 \cdot 10^{-3} \text{ °C}^2$.

and $V(s_i + h_j)$ are the parameter values at the positions (s_i) and $(s_i + h_j)$ separated by one specific lag distance h_j . For an irregularly spaced sample also a lag tolerance is introduced. That is, for a certain lag distance not only measurements at exactly the distance h_j but at $h_j \pm$ half the lag separation distance h_{sep} are considered.

The experimental semivariogram was calculated for each wall and for each parameter by an IDL routine written by James
 5 McCreight from the University of Colorado in 2008⁷ after the projected measurements of the corresponding parameter were detrended. In general, the semivariogram describes the correlation between different points at different distances.

To this experimental semivariogram, a commonly used exponential model function (e.g., after Isaaks and Srivastave, 1989) was fitted (Fig. 3, red solid line) which yields the necessary parameters range, nugget and (partial) sill:

$$\text{model} = \text{nugget} + \text{partial sill} \cdot \left[1 - e^{-\frac{3h}{\text{range}}} \right] \quad (3)$$

- 10 In this model, the value of the nugget is given by the value of the experimental semivariogram at the origin, the value of the sill corresponds to the sum of the nugget and the fitted parameter partial sill, and the range is defined as the lag distance h at which 95 % of the sill is achieved (Journel and Huijbregts, 1978).

The parameters from the exponential model are used to estimate the value $V(s_0)$ of the parameters, e.g., the dry gas mixing ratio of CH₄, at a position s_0 where no measurement was acquired based on the measured surrounding values $V(s_i)$ at the

⁷https://github.com/mccreigh/idl_variogram, last access: 06.07.2016

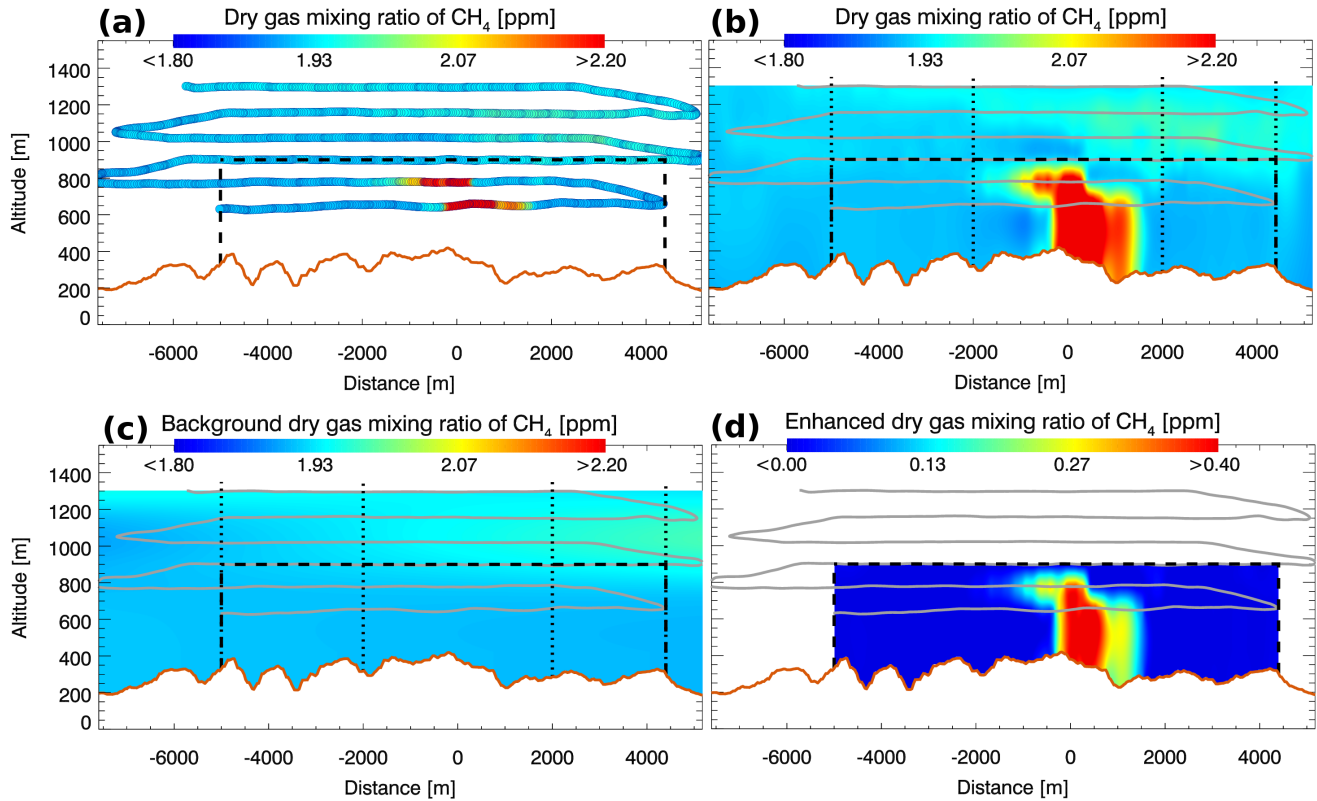


Figure 4. Example dry gas mixing ratios of CH₄ for the first downwind wall measured on the 01.09.2014 (middle in-situ wall in Fig. 5, solid red line). (a) Projected and time lag corrected mixing ratios acquired along the flight track onto the wall. (b) Kriged mixing ratios based on the measurements in (a) and an additionally added pseudo-track (not shown, see Sect. 6.2 for details). (c) Derived background mixing ratios from (b). (d) Derived CH₄ enhancement (kriged mixing ratios in (b) minus background mixing ratios in (c)). X-axis gives the distance from the approximate plume centre in m and y-axis gives the altitude in m above sea level (m asl). Solid orange lines depict the surface elevation (based on SRTM) and solid grey lines the projected flight track. Vertical dotted black lines show horizontal limits, which were used to define the background area (here: from -5.0 to -2.0 km and from 2.0 to 4.4 km). The area, which was used in the mass balance approach for estimating the emission rate, is enclosed by the dashed black lines.

positions s_i :

$$V(s_0) = \sum_{i=1}^n w_i \cdot V(s_i) \quad (4)$$

The influence of measured values $V(s_i)$ on the result is described by the respective weights w_i , whereas n is the total number of measurements. The weights are determined on basis of the above calculated parameters for the exponential model and the distances between the measured values and the unknown value, respectively (for further details, see Isaaks and Srivastave, 1989). Equation 4 is evaluated for each grid point on the plane surface.



For computation, the Kriging procedure ‘Krig_2D’ from IDL 8.2.3 was used⁸. An example of such a kriged in-situ wall is shown in Fig. 4 (b) for CH₄ measurements of the first downwind wall on the 01.09.2014.

Subsequently, the mass transport of CH₄ through each wall is estimated by a mass balance approach:

$$F_{IS} = \Delta z \cdot \Delta x \cdot f_{IS} \sum_i (c_i - c_{0,i}) \cdot \frac{p_i}{T_i \cdot k_B} \cdot u_{eff,i} \quad (5)$$

- 5 where i is the index representing the i^{th} grid box, c is the measured CH₄ concentration in $\mu\text{mol mol}^{-1}$ or ppm, c_0 is the CH₄ background concentration in $\mu\text{mol mol}^{-1}$ or ppm, p is the pressure in Pa, T the ambient temperature in K, k_B the Boltzmann constant, Δz and Δx are the vertical (in altitude) and horizontal extents of the grid boxes in m, respectively, f_{IS} is a conversion factor having the same value and units as f_{RS} in Eq. 1 in order to retrieve the emission rate F_{IS} in $\text{kt CH}_4 \text{ yr}^{-1}$, and u_{eff} is the effective wind speed in m s^{-1} . The effective wind speed accounts for the wind speed normal to the plane surface and a geometry
- 10 factor which considers the orientation of the wall relative to the orientation and flight direction of the aircraft, respectively, while a single measurement is recorded, and the wind direction. If the fitted wall is parallel to the measurement or perpendicular to the wind direction, the geometry factors becomes 1. The concentration c , the temperature T and the effective wind speed u_{eff} are based on Kriging, whereas the pressure $p = p(z)$ only depends on the altitude of the grid box i . The functional dependency $p(z)$ has been determined beforehand by fitting a linear function to the projected pressure measurements.
- 15 As indicated by Eq. 5, only the CH₄ enhancement above the background is needed. In order to separate the plume signal from the background, the plane surface of the CH₄ measurements is segmented into a plume area and a background area (Fig. 4, (b)). For each altitude level, a linear function is fitted to the CH₄ measurements in the background area by a least-squares approach. This yields a 2D-distribution of the CH₄ background for the specific in-situ wall (Fig. 4, (c)). Subtracting the achieved CH₄ background from the plane surface of the CH₄ measurements results in the pure CH₄ signal (Fig. 4, (d)) originating from the
- 20 source under consideration. This method accounts for possible concentration gradients in the CH₄ background in the horizontal and vertical direction.

5.3 Retrieval of CH₄ anomaly maps by AVIRIS-NG data

- AVIRIS-NG methane retrievals use a matched filter approach previously demonstrated in campaigns at Kern River (Thompson et al., 2015), Four Corners (Frankenberg et al., 2016), and Aliso Canyon (Thompson et al., 2016). We treat AVIRIS-NG
- 25 spectra x as Independent Identically Distributed (IID) instantiations of a multivariate Gaussian distribution with mean μ and covariance matrix Σ , written $x \sim \mathcal{N}(\mu, \Sigma)$. To account for the independent noise properties of each detector element, we model the spectra from each pushbroom element separately. This produces a slightly different distribution for every cross-track position. The covariance matrices are regularized to ensure accuracy and numerical stability for the limited number of samples.

⁸<http://www.harrisgeospatial.com/docs/krig2d.html>, last access: 04.03.2016



For each new spectrum, the matched filter estimates the magnitude α of a linear perturbation of this Gaussian distribution in the direction of the target signal. The estimate $\hat{\alpha}(x)$ is written:

$$\hat{\alpha}(x) = \frac{(x - \mu)^T \Sigma^{-1} t}{t^T \Sigma^{-1} t} \quad (6)$$

Here the target is the radiance Jacobian with respect to a change in CH₄ absorption above background. The magnitude of the resulting estimate indicates the enhancement of CH₄ absorption above the local background in units of ppm × meters. After detection, the resulting maps are georectified to permit direct comparison with MAMAP retrievals using synchronized IMU/GPS data and a local digital elevation model.

6 Results

6.1 Emission rates from MAMAP remote sensing data

Remote sensing measurements over the Olinda Alpha Landfill were collected on four different days (27.08.2014, 28.08.2014, 01.09.2014, 03.09.2014) by the MAMAP remote sensing instrument. A detailed list of flight parameters, which were used for the radiative transfer model simulations using SCIATRAN (Rozanov et al., 2014) to generate the look-up table, are found in Table 1 for each day.

For the emission rate estimates, only flight tracks located downwind of the landfill were used. A detailed error discussion is given in Sect. 6.1.1.

The flight altitude on the four days varied between 1630 and 1970 m asl, the surface elevation was around 300 m asl, the flight speed was around 60 m s⁻¹ and the total measurement time per ground sample was around 0.8 s. The ground scene size for a general flight altitude of around 1800 m asl and this speed in combination with the surface elevation is approximately 69 × 60 m² (cross track × along track) for a focal length of the installed front optics of $f = 100\text{ mm}$.

For the remote sensing measurements on the 01.09.2014, the wind direction was estimated to be 241° which is in good agreement with the in-situ based wind direction of 238° derived from in-situ measurements at the plume location of the second downwind wall (dw2 in Fig. 5, solid red line; for details of the definition of the plume location, see Sect. 6.2), which was flown directly after the remote sensing pattern. The wind speed was around 4.4 m s⁻¹ determined over the same area as for the wind direction. An overview of the flight pattern and the measured CH₄ column enhancements is given in Fig. 5. In addition to a clear plume signal observed up to 8 km downwind of the landfill, some CH₄ depletions are visible in the collected data. The origin of these negative CH₄ anomalies will be further discussed in Sect. 6.1.2.

For the emission retrieval, the area between -1750 and -4000 m (measurements south of the plume between the yellow lines in Fig. 5, left) and +1750 and +4000 m (measurements north of the plume between the yellow lines in Fig. 5, left) was used for background concentration normalization (also compare to Fig. 6, a). The mean emission rate estimate derived from Eq. 1 applied to the 13 downwind tracks (Fig. 6, a) is 13.9 kt CH₄ yr⁻¹.



Table 1. Flight conditions and MAMAP remote sensing parameters for the four flights.

Flight day	27.08.2014	28.08.2014	01.09.2014	03.09.2114
Flight time (local time)				
start [hh:mm]	14:11	14:21	14:55	13:27
end [hh:mm]	14:55	15:07	16:05	14:14
Solar zenith angle (SZA)				
min [°]	29.9	31.7	38.3	27.6
max [°]	37.0	39.3	51.3	32.6
Flight altitude [m]	1971	1627	1794	1945
Surface elevation along flight track				
min [m]	80	81	109	114
max [m]	437	435	483	496
Mean column mixing ratios				
CH ₄ [ppb]	1744.5	1750.1	1807.3	1795.6
CO ₂ [ppm]	396.8	396.0	391.7	393.1
Aerosol scenario [–]	urban	urban	urban	urban
Albedo [–]	0.31	0.31	0.31	0.31
Wind speed [m s ^{–1}]	6.3	8.2	4.4	5.6
Wind direction				
empirical (center line) [°]	236	240	241	240
in-situ [°]	238	247	238	259

The MAMAP measurements on 03.09.2014 were treated in a similar way as for the 01.09.2014 flight. The wind direction was 240° based on the empirical center line of the plume (measured in-situ wind direction is 259°). The wind speed was 5.6 m s^{–1}. Figure S3 shows the flight pattern and the CH₄ column enhancements.

In order to estimate the emission rate, the data was again filtered by the basic signal strength filter and by inclination. In contrast to the 01.09.2014, the area used for background normalization was set empirically for each track because the flight tracks were quite short near the source and longer further away. This was done on basis of the observed plume signal seen in the cross sections (Fig. S4, right column), whereby a broadening of the plume, while moving away from the source, was also considered. Additionally, the maximal width of the plume area of the latter remote sensing tracks was further constrained by the approximate plume width observed in the in-situ measurements. The mean emission based on the 8 downwind tracks is 16.4 kt CH₄ yr^{–1}.

The 27.08.2014 and 28.08.2014 flights are more challenging with respect to the flux inversion because of the not optimal flight patterns. This resulted in there being few measurements for concentration background normalisation and a non-optimal orientation of the flight tracks with respect to the prevailing wind direction. Additionally, higher wind speeds potentially lead

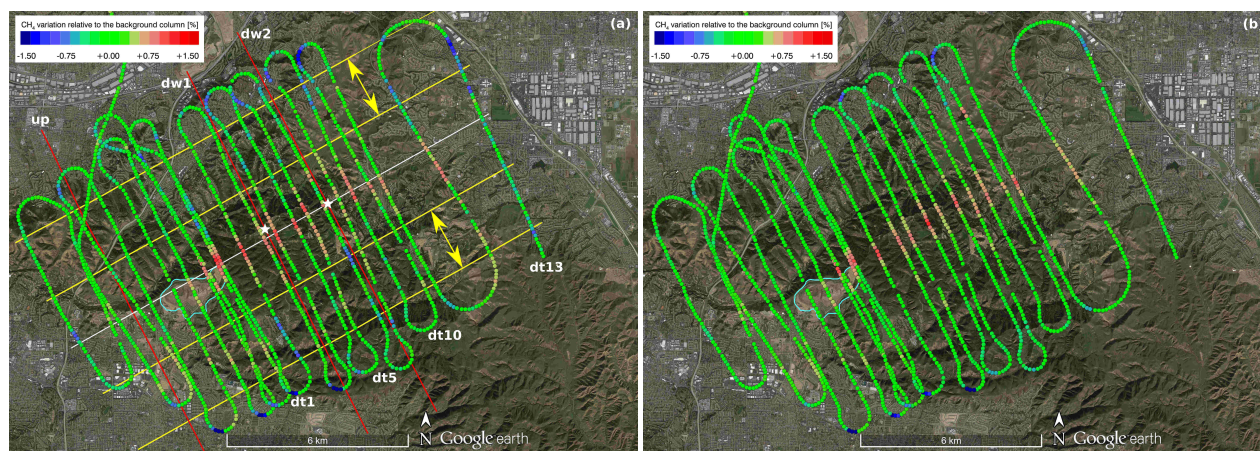


Figure 5. The complete MAMAP remote sensing flight pattern without the inclination filter over the Olinda Alpha Landfill (encircled by the cyan solid line) on 01.09.2014 is shown. The $\text{XCH}_4(\text{CO}_2)$ data is smoothed by a 3-point moving average and normalized by a 300-point moving average for visualisation purpose only. (a) For references, the positions of the center line (solid white line), the normalisation areas (area between the solid yellow lines emphasized by the yellow arrows), the three flown in-situ walls (solid red lines; upwind wall, up; first downwind wall, dw1; second downwind wall, dw2) and labels for the thirteen remote sensing downwind tracks (dt1 to dt13) are also depicted. The white stars emphasize the location of the approximate in-situ plume location, which corresponds to the origin used in Figs. 4, S7 (c-f) and S9 (c,d). (b) Signal strength dependency corrected measurements (for details, see Sect. 6.1.2). The map underneath is provided by Google Earth.

to smaller column enhancements. The flight parameters are listed in Table 1, Figs. S1 and S2 show the flight pattern and Fig. S4 (left and middle column) the downwind tracks.

On the 27.08.2014, the area used for background normalization was empirically set and also additionally constrained by the approximate plume width estimated from the in-situ measurements. In contrast to the remaining flights, the inclination filter was relaxed to 6° to increase the number of measurements north of the observed plume. Analysis using the 5 downwind tracks yields a mean emission of $13.0 \text{ kt CH}_4 \text{ yr}^{-1}$.

The 28.08.2014 flight was treated in a similar manner to the flights before using again the standard inclination filter of 5° . The resultant mean emission rate from the 6 downwind tracks is $13.7 \text{ kt CH}_4 \text{ yr}^{-1}$. A detailed error discussion is given in Sect. 6.1.1.

6.1.1 Uncertainty of estimated MAMAP remote sensing emission rates

The largest errors or uncertainties for the remote sensing based emission estimates originate from uncertainties of the wind parameters used (wind speed and direction), the chosen concentration background normalisation area, the track-to-track variability and the influence of CO_2 variations in terms of the applied $\text{XCH}_4(\text{CO}_2)$ proxy method. Uncertainty estimates for these error sources are listed in Table 2. A detailed error discussion of the different error sources is given in the following.

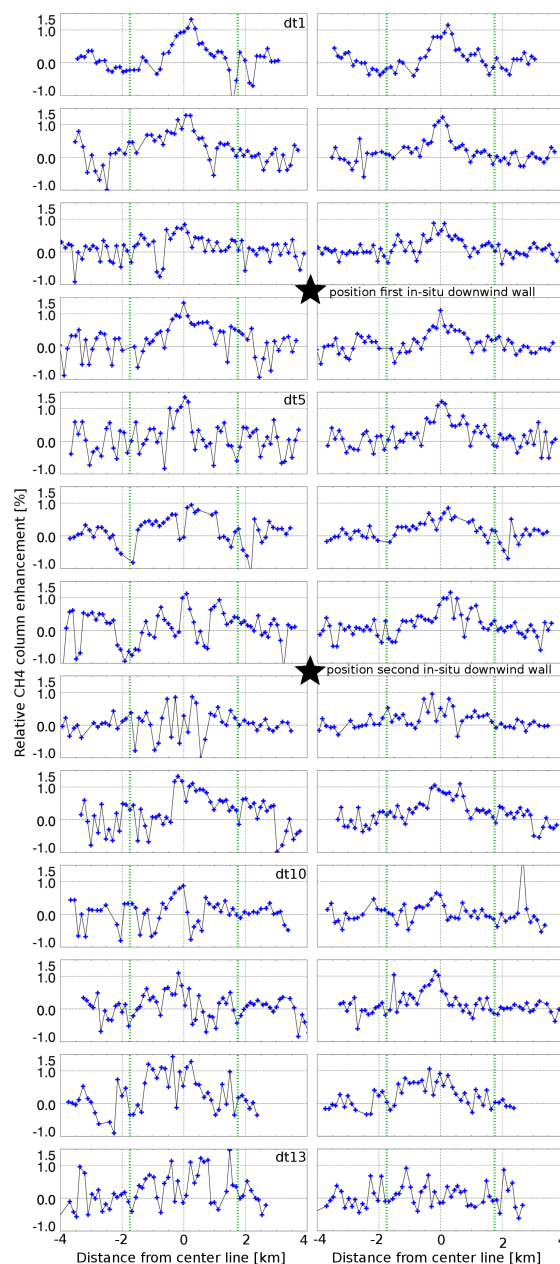


Figure 6. Shown are the 13 downwind tracks (filtered for signal strength and inclination, dt1 to dt13) from the MAMAP remote survey over the Olinda Alpha Landfill on 01.09.2014, which were used for the emission rate estimate using Eq. 1. The x-axis depicts the distance from the centre line in km (see also Fig. 5, white solid line) and the y-axis gives the CH_4 column enhancement relative to the background column. The area on the left (-4.0 to -1.75 km) and right (+1.75 to +4.0 km) side of the dotted green line was used for background normalisation. Left column: Non-corrected measurements. Right column: Signal strength dependency corrected measurements (see Sect. 6.1.2 for details).



A wind speed error linearly propagates into the emission estimate. As the in-situ measurements of the 5-hole turbulence probe were utilized for the wind speed estimates, the accuracy of the probe is used as a first order approximation for an uncertainty estimate. The uncertainty of the turbulence probe wind speed data is 0.5 m s^{-1} . The resulting uncertainty on the estimated flux is around $\pm 11 \%$ and $\pm 9 \%$ for the 01.09.2016 and 03.09.2016 flight, respectively. The uncertainty is slightly
 5 smaller on the 27.08.2014 ($\pm 8 \%$) and on the 27.08.2014 ($\pm 6 \%$) (compare to Table 1) as a results of the higher wind speeds.

The wind direction enters the flux estimate via a cosine term by modifying the used perpendicular wind speed to each flight track, provided that the track orientation is not perpendicular to the mean wind direction. An error on the wind direction of $\pm 10^\circ$ has been assumed for the case when wind direction is derived from the measurements themselves.

On the 01.09.2014, the remote sensing tracks were flown nearly perpendicular to the estimated prevailing wind direction
 10 with an average deviation of only 3° . The assumed error in the wind direction of 10° leads to an uncertainty in the emission estimate of up to 2% . For the 03.09.2014 flight, the mean deviation from the perpendicular wind direction was around 13° leading to a maximum emission uncertainty of 6% . The largest mean deviation from the perpendicular wind direction of around 60° is observed on the 27.08.2014. For a $\pm 10^\circ$ wind direction uncertainty, this leads to an uncertainty in the emission rate of maximal 22% . On the 28.09.2014, the deviation of around 35° with respect to the perpendicular wind direction was smaller in
 15 comparison to the 27.08.2014 flight leading to a maximal uncertainty in the emission rate of 14% .

When inspecting the downwind tracks used for the emission estimates in, e.g., Figs. 5 and 6 for the 01.09.2014, it becomes obvious that the limits for the background normalisation area also have an influence on the final results. In order to test their impact on the final emission estimate, the limits were shifted towards or away from the center line by a certain distance. For this type of test, one needs to keep in mind that if the limits are too close to the plume, part of the plume signal enters the
 20 area used for the background normalization leading to an underestimate of the emission. On the other hand, if the limits are too far away, there might be not sufficient measurements left to calculate a reliable concentration background. Thus, the limits were varied by ± 250 and $\pm 500 \text{ m}$ and, additionally, the defined plume area was shifted as a whole by 250 and 500 m to the right and left with respect to the center line. This yields a maximal change in the emission of around 19% and 18% for the 01.09.2014 and the 03.09.2014, respectively. For the 27.08.2014 and 28.08.2014, the maximal uncertainty in the emission rate
 25 is around 34% and 29% , respectively.

Additionally, we computed the statistical error contribution. This error source is referred to as track-to-track variability in the following. Based on the used downwind tracks, a standard deviation σ and from that the uncertainty of the mean, is calculated. This yields a $1-\sigma$ uncertainty of $\pm 6.9 \text{ kt CH}_4 \text{ yr}^{-1}$, or $\pm 50 \%$ of the derived mean emission rate, for a single track and an error on the averaged emission of around $\pm 14 \%$ when using the 13 downwind tracks (for further details, see Farrance and
 30 Frenkel, 2012) on the 01.09.2014. On the 03.09.2014, the observed $1-\sigma$ track-to-track variability is $\pm 5.3 \text{ kt CH}_4 \text{ yr}^{-1}$ (or $\pm 32 \%$) based on eight tracks yielding an error of around $\pm 11 \%$ on the mean emission rate. The track-to-track variability is $\pm 4.6 \text{ kt CH}_4 \text{ yr}^{-1}$ (or $\pm 35 \%$) on the 27.08.2014 leading to an error on the average of around $\pm 16 \%$ considering the five downwind tracks. On the 28.08.2014, the track-to-track variability of the six downwind tracks is $\pm 6.3 \text{ kt CH}_4 \text{ yr}^{-1}$ (or $\pm 46 \%$) causing an error on the average of around $\pm 19 \%$ in the emission rate estimate.

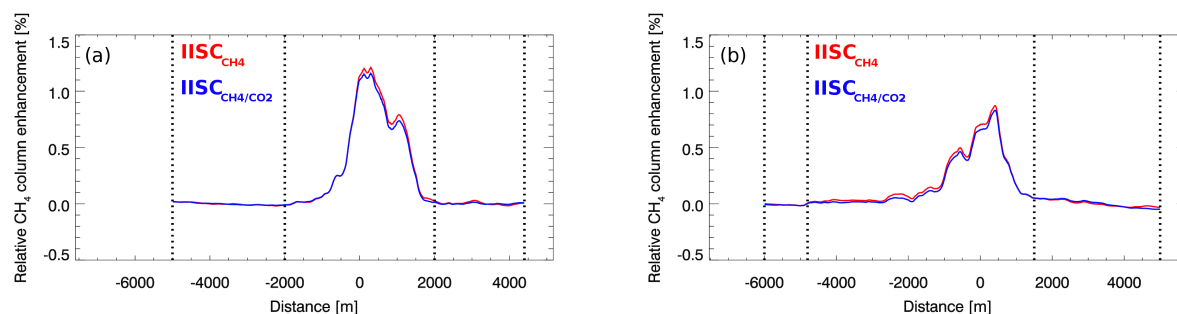


Figure 7. Cross-sections of the relative CH_4 column enhancements determined from the integrated in-situ columns (IISCs) of the first (a) and second (b) downwind wall of the Olinda Alpha Landfill measurements on 01.09.2014. The blue solid lines ($\text{IISC}_{\text{CH}_4/\text{CO}_2}$) represent the cases which are influenced by the co-emitted CO_2 , whereas the red solid lines ($\text{IISC}_{\text{CH}_4}$) are not. The measurements enclosed by the black dotted lines and located at the flanks / edges of the plume are used for normalization and determination of the background.

For the remote sensing emission rate estimate, the $\text{XCH}_4(\text{CO}_2)$ columns, determined using the proxy method, are used. The proxy method assumes that CO_2 was equally distributed and did not change in the measured area during the flight. In general, any CO_2 enhancement would lead to a decline in the derived $\text{XCH}_4(\text{CO}_2)$. The influence of such a CO_2 anomaly on the emission rate estimate depends on its location. On the one hand, the CO_2 enhancements can be co-located to the CH_4 landfill plume for the case when the CO_2 is co-emitted. This will lead to an underestimation of the emission rate. On the other hand, if the CO_2 originates from outside the measurement area, the enhancement is not co-located to the CH_4 plume. This results in an under- or overestimation of the emission rate depending on the location and distribution of the CO_2 variations.

To estimate the influence of a variable CO_2 concentration in the measurement area on the remote sensing emission rate estimates, integrated in-situ columns (IISCs) were derived for the measured in-situ walls. The in-situ CH_4 and CO_2 measurements were vertically integrated from the surface to highest altitude of the in-situ wall. Subsequently, the two obtained IISCs for CH_4 and CO_2 were similarly treated as they would be in the MAMAP proxy approach. First, the CH_4 column was divided by the CO_2 column and then the track was background normalized by its edges. This results on the one hand in an $\text{IISC}_{\text{CH}_4}$ from the CH_4 enhancement only, which is not influenced by CO_2 variations, and on the other in an $\text{IISC}_{\text{CH}_4/\text{CO}_2}$ which considers CO_2 variations.

Figure 7 shows exemplarily the background normalized IISCs of the two downwind walls on the 01.09.2014 for the background normalized $\text{IISC}_{\text{CH}_4}$ (red solid line) and $\text{IISC}_{\text{CH}_4/\text{CO}_2}$ (blue solid line). On that day, the CO_2 plume is co-located to the CH_4 plume and causes a reduction of the CH_4 plume signal. This finding is consistent with the kriged CH_4 and CO_2 in-situ measurements in Figs. S7 (d,f for CH_4) and S12 (d,f for CO_2), which show a well-defined CO_2 enhancement at the position of the methane plume.

To quantitatively estimate the influence of this offset on the final emission rate estimate, the emission through each in-situ based cross-section $\text{IISC}_{\text{CH}_4}$ and $\text{IISC}_{\text{CH}_4/\text{CO}_2}$ is calculated by using Eq. 1. The column enhancement V and the length segment



Δx are given by Fig. 7, whereby the remaining parameters, especially the perpendicular wind speed, cancel out, because we are only investigating in the relative difference.

On the 01.09.2014, the derived emission rates are by around 5.0 % (first downwind wall) to 11.7 % (second downwind wall) higher if the influence of the CO₂ on the emission rate is neglected.

- 5 Assuming that this in-situ based derived bias is valid for the entire measurement area, which is covered by the remote sensing instruments, indicates that the emission rate estimates based on the remote sensing data are also underestimated by around 5.0 % to 11.7 % due to the co-located CO₂ on the 01.09.2014.

Applying this method to the other downwind walls yields around +1.7 % (27.08.2014), -15.8 % (28.08.2014) and +3.6 % (03.09.2014). The IISCs of these walls are found in the supplement (Figs. S14, S15 and S16). Strictly speaking, due to the
 10 potential temporal and spatial variability of the CO₂ variations, these calculated biases estimated from the downwind walls are not assumed to be valid for the remote sensing tracks of the associated flight day, which were recorded at a different time and location. Therefore, we used the 1- σ deviation of the derived biases to estimate one uncertainty of around ± 10 % for the entire remote sensing data set.

The total uncertainties were calculated by root-sum-squaring the single uncertainties for each day with the underlying as-
 15 sumption that the error sources are not correlated. The resulting total uncertainties including the uncertainties in wind information, normalization area, track-to-track variability and CO₂ variations, of the remote sensing measurements for the 01.09.2014, 03.09.2014, 27.06.2014 and 28.06.2014 are 28 % (or 3.9 kt CH₄ yr⁻¹), 26 % (or 4.3 kt CH₄ yr⁻¹), 46 % (or 5.9 kt CH₄ yr⁻¹) and 39 % (or 5.3 kt CH₄ yr⁻¹), respectively.

6.1.2 Non-linearity and associated negative XCH₄ anomalies

- 20 When investigating the MAMAP remote sensing measurements on the 01.09.2014 (Fig. 5, a), they also show, besides a clear plume structure downwind of the landfill, some blue spots. First investigations have revealed some column dependencies on the signal strength. The scatter plot in Fig. 8 shows the ratio of the retrieved CH₄ and CO₂ profile scaling factors as a function of signal strength. It (black diamonds) clearly shows a decrease in the ratio for lower signals and also a less pronounced decrease for higher signal strengths. The cause of this dependency is still under investigation. The effect is most pronounced on the
 25 01.09.2014 flight having the most measurements at lower signal strengths (e.g., 32 % below 13000 counts) with respect to the three other days (5 % on 27.08.2014, 12 % on 28.08.2014 and 2 % of the measurements on 27.08.2014). Therefore, the effect is further investigated exemplarily for the 01.09.2014.

In order to test the hypothesis that the negative XCH₄(CO₂) anomalies originate from this signal dependency on the 01.09.2014, a 3rd order polynomial (Fig. 8, red solid line) was fitted to the scattered data and subsequently used for cor-
 30 rection. The new data set exhibits nearly no signal strength dependency (Fig. 8, green diamonds). Furthermore, the blue spots in Fig. 5 (b) are reduced compared to Fig. 5 (a). The 1- σ track-to-track variability of ± 6.9 kt CH₄ yr⁻¹ has also been reduced by 26 % to about ± 5.1 kt CH₄ yr⁻¹ (or ± 37 %).

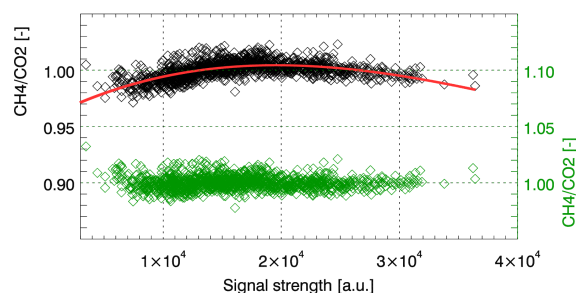


Figure 8. Scatter plot of the ratio of the retrieved CH₄ and CO₂ column over the maximum signal strength on the 01.09.2014. Black diamonds: Non-corrected data, left scale. Red solid line: Fitted 3rd order polynomial. Green diamonds: Corrected data, right scale.

It is expected that this effect was less relevant for measurements from previous campaigns because the measured radiance signals and column enhancements were significantly higher than here. The mean emission changes furthermore by less than 2 % for the investigated Olinda Alpha Landfill measurements on the 01.09.2014 due to this effect and can therefore be neglected.

6.2 Emission rates from Picarro in-situ data

- 5 For comparison with the MAMAP remote sensing estimates, CH₄ emission rates from the Olinda Alpha Landfill were also derived from consecutive in-situ measurements made by the Picarro instrument performed with the same aircraft for each of the four days, where MAMAP remote sensing data was acquired. In total, five in-situ walls were flown downwind of the landfill during the period. The emission rate estimates for each wall have been calculated using the Kriging and mass balance method as described in Sect. 5.2. The downwind walls of the dry gas mixing ratios of CH₄ and the effective wind speeds obtained by
- 10 Kriging can be found in the supplement (Sect. S2 and S4).

For the lag separation distance h_{sep} (see Sect. 5.2), a value of 40 m, leading to a lag tolerance of 20 m, was chosen for calculating the experimental semivariograms. This value is based on the Picarro instrument, which is the „slowest“ in-situ instrument, whose measurements are used in Eq. 5 for the emission rate estimate. The Picarro greenhouse gas sensor acquires measurements at around 1.7 Hz, corresponding to a measurement every 0.6 s. In combination with the flight speed of the

15 aircraft of around 60 m s⁻¹, this leads to a spatial resolution of around $\lesssim 40$ m. To cover at least one pair of measurements per lag distance h_j , a lag separation distance h_{sep} of around 40 m is needed.

For fitting the exponential model to the experimental semivariograms, only half of the maximum possible lag distance (largest distance by which a pair of measurements on the wall is separated) has been used following the recommendations in Journel and Huijbregts (1978). Figure 3 shows an example of an experimental semivariogram with the fitted exponential

20 function and the related parameters range, nugget and partial sill.

As mentioned in Sect. 4, to account for the fact that measurements are not available at the surface, a pseudo-track is added at the surface. It follows the surface terrain and, in a first order approximation, has the same concentration values of CH₄



Table 2. Summary of the derived emission rates denoted as 'retrieved baseline' and their related relative errors from the remote sensing (RS) and in-situ (IS) data set of the Olinda Alpha Landfill measurements.

Error type		27.08.2014	28.08.2014	01.09.2014	03.09.2014
RS	Retrieved baseline [kt CH ₄ yr ⁻¹]	13.0	13.7	13.9	16.4
	Wind speed [%]	7.9	6.1	11.4	9.0
	Wind direction [%]	22.2	13.7	2.4	5.5
	Background normalization area [%]	34.1	29.0	18.6	18.1
	Track-to-track variability [%]	15.7	18.7	13.9	11.4
	Background CO ₂ variation ^{a)} [%]	10.3	10.3	10.3	10.3
Total uncertainty [%]		45.5	39.0	27.9	26.0
IS ^{b)}		dw1	dw1	dw1 dw2	dw1
	Retrieved baseline [kt CH ₄ yr ⁻¹]	12.0	16.8	18.2 14.8	13.8
	Group a) Wind speed [%]	12.4	6.3	14.4 12.6	10.4
	Unknown surface concentrations [%]	5.2	8.1	15.8 10.0	13.1
	Time lag [%]	10.1	8.4	6.6 1.8	4.1
	Group b) Kriging parameters [%]	4.6	7.7	16.2 2.8	9.1
	Background concentrations / area [%]	2.6	6.8	2.9 7.3	2.5
Total uncertainty [%]		17.6	16.8	27.8 18.0	19.6

^{a)} based on the CH₄ and CO₂ in-situ measurements

^{b)} dw = downwind wall

and CO₂ as measured at the altitude of the lowest flight track of the according wall. The surface winds for the pseudo-track were estimated from measurements of the weather station MTNRC1⁹ located at the north eastern tip of the Olinda Alpha Landfill. The resulting surface wind speeds and directions at the time the downwind walls were acquired are 5.8 m s⁻¹ and 219° (27.08.2014), 5.9 m s⁻¹ and 228° (28.08.2014), 4.5 m s⁻¹ and 209° (dw1, 01.09.2014), 4.5 m s⁻¹ and 209° (dw2, 01.09.2014), and 4.9 m s⁻¹ and 220° (03.09.2014). This pseudo-track is used to extrapolate the measurements and close the gap between the lowest flight leg and the surface.

The mean perpendicular wind speeds for the five downwind walls measured on the four days varied between 3.5 and 8.0 m s⁻¹, retrieved from the measurements by the 5-hole turbulence probe and the surface weather station. These averaged wind speeds were calculated from all grid boxes, which exhibit a CH₄ enhancement larger than three times the standard deviation of the CH₄ signal in the background area. Subsequently, the wind speeds were also weighted by the amount of the enhanced CH₄ molecules in the respective grid boxes. The average area, for which the mean perpendicular wind speeds were

⁹<https://www.wunderground.com/personal-weather-station/dashboard?ID=MTNRC1#history>, last access: 16.11.2016



calculated over, was around $1.0 \times 1.0 \text{ km}^2$. This method was chosen to select the wind measurements, which belong to the CH_4 plume signal. The $3\text{-}\sigma$ threshold has also been used previously as limit for identifying and distinguishing plume signals from the surrounding background (e.g., Hörmann et al., 2013; Zien et al., 2014).

The resulting emission rate estimates calculated by Eq. 5 vary between 12.0 and 18.2 kt $\text{CH}_4 \text{ yr}^{-1}$ during the one week of measurements (see Table 2 for details). When inspecting the three available in-situ upwind walls (Figs. S5 (b), S6 (b) and S7 (b)), it becomes clear that the calculated emissions are a feature of the emissions from the Olinda Alpha Landfill and are not an artefact of inflow of polluted air masses. The upwind walls do not exhibit any noticeable CH_4 enhancements or structures.

6.2.1 Airborne in-situ error analysis

For the error budget of the in-situ based emission rates, two groups of error sources have been identified: a) measurement related uncertainties and b) method related uncertainties. In the following, the different error sources are exemplarily discussed for the measurements on 01.09.2014. A summary of all errors for the 5 downwind walls measured on the four different days is given in Table 2.

The main contributor to group a) is the measurement of the wind speed by the 5-hole turbulence probe of the CIRPAS instrumentation. Any error in the wind speed linearly propagates to the emission estimate (compare to Eq. 5). Using the averaged perpendicular wind speeds of the first (3.5 m s^{-1}) and second (4.0 m s^{-1}) downwind wall on 01.09.2014, an accuracy of 0.5 m s^{-1} translates into an uncertainty in the emission estimate of around $\pm 14\%$ and $\pm 13\%$, respectively. However, this is a slight overestimation because the error is not related to the larger absolute wind speed in wind direction but to the smaller perpendicular wind calculated relative to the fitted wall.

The second largest error originates from the lack of measurements down to the surface. It was assumed as baseline that the plume had been well-mixed in the lower part of the atmospheric boundary layer. Due to the hilly area, accumulation of CH_4 in the valleys or lifts off could potentially also be possible. To quantify these effects, it was assumed that the pseudo-surface track used for extrapolation contains 50 or 150 % of the CH_4 enhancements with respect to the lowest observed flight track. This yields emissions which deviate by maximal around $\pm 16\%$ for the 01.09.2014.

A third error source originates from the time lag, which is around 21 s. The sensitivity of the final emission estimate to a variation of the time lag by $\pm 5 \text{ s}$ is maximal 7 % for the 01.09.2014.

Group b) consists of errors which originate e.g. from the chosen interpolation technique “Kriging” and how these data are used in the mass balance approach.

As discussed in the previous section, the Kriging method requires the three parameters nugget, (partial) sill and range, which were derived beforehand by fitting an exponential function to the experimental semivariogram for each quantity used in the mass balance approach. To quantify the influence of the Kriging parameters on the estimated emission and how sensitive it responds, the range was varied by a factor of 4 (i.e., -75% and $+300\%$). Additionally, six configurations for the parameters nugget and partial sill (bearing in mind that the sill is the sum of partial sill and nugget) were investigated. On the one hand, the nugget was set to zero so that the partial sill equalled the sill and on the other hand, the nugget was increased to half of the sill and the partial sill was decreased to half of the sill. This was done for three different sills: the standard derived sill, two



times the standard derived sill and half the standard derived sill. Furthermore, the effect of a varying lag separation distance, which also slightly influences the fitted parameters, is covered.

Varying Kriging parameters for the two quantities wind speed and CH₄ concentration have the largest influence on the final emission estimate, whereby the effect of temperature is negligible. The Kriging error results in a flux uncertainty of at most 16 % for the 01.09.2014. These tests show, that the influence of the Kriging parameters on the emission is comparable to other error sources but can also be one order of magnitude smaller. It is also important to emphasize, that the chosen values likely reflect the maximum deviations from the derived ones. When inspecting the experimental semivariograms in Fig. 3 it becomes obvious that, e.g., a nugget and partial sill value of 50 % of the sill or, e.g. in case of temperature, a range reduced to 0.23 or increased to 3.6 km (fitted value is 0.9 km for temperature), respectively, is quite unlikely. Therefore, it is expected, that the real uncertainty originating from the Kriging parameters is smaller.

A further error source originates from the limits for the background area. To test its sensitivity, the limits have been varied till their size had only 50 % of the original size. The resulting emission deviates by up to around 3 % and 7 % for the first and second downwind wall, respectively, on the 01.09.2014.

Combining the above mentioned error sources and calculating the root sum square error yields a total uncertainty of around 28 % (first downwind wall) and 18 % (second downwind wall) for the flight on the 01.09.2014. The uncertainties for the three other flight days are listed in Table 2.

6.3 CH₄ anomaly maps obtained by the AVIRIS-NG instrument

Airborne remote sensing measurements by the AVIRIS-NG imaging spectrometer were performed on the 03.09.2014. The instrument acquired five flight lines over the landfill at an flight altitude of around 3 km agl between 13:30 and 14:10 local time. The flight lines have a length of approximately 9 km and a swath of around 1.8 km resulting in a fine spatial resolution of around $3 \times 3 \text{ m}^2$. Figure 9 shows the derived CH₄ anomaly map of one flight line in the near field of the landfill using the algorithm described in Sec. 5.3. The remaining flight lines, observed by the AVIRIS-NG instrument, are found in Fig. S17 in the supplement. It shows a clear plume structure developing at the south-western slope of the landfill. This plume is also visible in the CH₄ anomaly maps for the multiple AVIRIS-NG overpasses (see supplement Fig. S17). Due to atmospheric variability, its shape and intensity changes from overflight to overflight, but the plume remains visible. However, surface structures / surface albedo effects can cause spurious signals, which in the most cases can be identified as such.

7 Comparison of emissions

7.1 Comparison between MAMAP remote sensing and Picarro in-situ data

The estimated emission rates of the Olinda Alpha Landfill from the airborne in-situ and remote sensing measurements agree well for the analysed days (see Fig. 10). Due to the time delay between the two surveys performed with both techniques and, thus, for example a possible change in wind direction, it is not expected that the location of the measured plumes is identical.

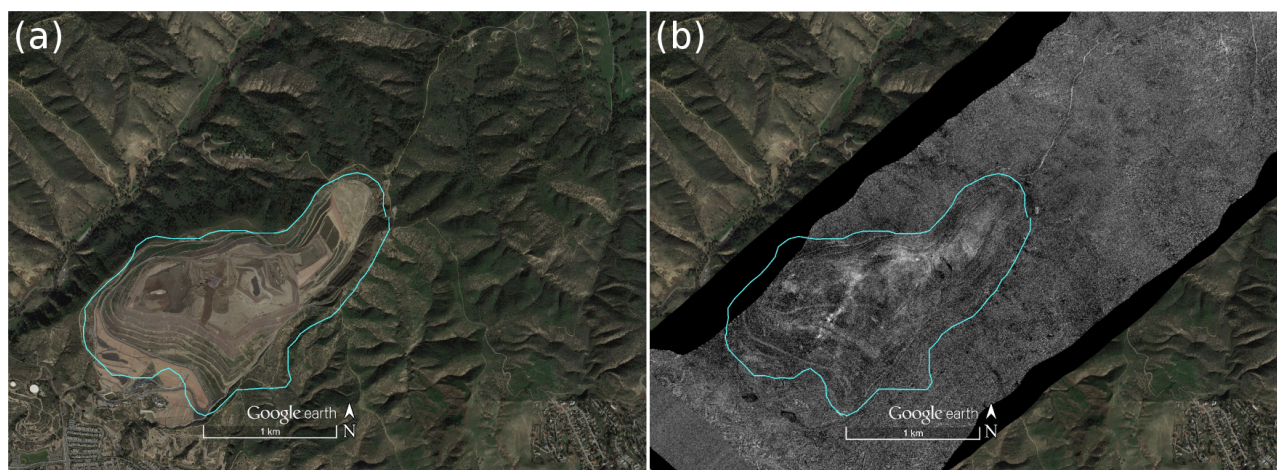


Figure 9. (a) Google Earth map showing the Olinda Alpha Landfill encircled by the cyan solid line. (b) CH_4 anomaly map derived from AVIRIS-NG data and superimposed on the Google Earth map. Shown is the near field around the landfill acquired at around 13:33 local time. White pixel corresponds to a detected CH_4 enhancement. Wind direction was approximately south-west. An enhanced version of the same flight line and view is shown in Fig. 11.

Nevertheless, the positions of the plumes observed by the remote sensing and in-situ instrument are in close vicinity to each other for each of the four days (see Figs. 5 (a), S1, S2 and S3).

On the 01.09.2016, the emissions derived from the two in-situ downwind walls are $18.2 \text{ kt CH}_4 \text{ yr}^{-1} (\pm 28 \%)$ and $14.8 \text{ kt CH}_4 \text{ yr}^{-1} (\pm 18 \%)$, respectively. The difference between the two walls is $3.4 \text{ kt CH}_4 \text{ yr}^{-1}$, whereas the average emission rate based on the two in-situ walls is around $16.5 \text{ kt CH}_4 \text{ yr}^{-1}$. As suggested in Cambaliza et al. (2014), the difference between the walls can be related to the average emission rate and be used as a measure for the precision of this method. For the flight on the 01.09.2014, this results in a difference of around 21 %, which is in good agreement with the values derived in Cambaliza et al. (2014) ranging from 12 % to 39 %. Furthermore, the averaged in-situ based emission rate is in good agreement with the remote sensing based emission of $14.9 \text{ kt CH}_4 \text{ yr}^{-1} (\pm 28 \%)$.

The in-situ and remote sensing based emission rates are also in good agreement on the 27.08.2014 (IS: $12.0 \text{ kt CH}_4 \text{ yr}^{-1} \pm 18 \%$, RS: $13.0 \text{ kt CH}_4 \text{ yr}^{-1} \pm 46 \%$) and 03.09.2014 (IS: $13.8 \text{ kt CH}_4 \text{ yr}^{-1} \pm 20 \%$, RS: $16.4 \text{ kt CH}_4 \text{ yr}^{-1} \pm 26 \%$).

The largest difference of around $3.1 \text{ kt CH}_4 \text{ yr}^{-1}$ is observed on the 28.08.2014. On that day, the highest wind speeds were observed potentially leading to smaller measured column enhancements with respect to the measurements performed on the other days. Therefore, the resulting signals are more difficult to detect by MAMAP and part of the plume signal might be obscured due to the statistical measurement noise (precision) of the instrument leading to an underestimate of the emission.

The average absolute difference between the emission rates based on remote sensing and in-situ is $2.4 \text{ kt CH}_4 \text{ yr}^{-1}$.

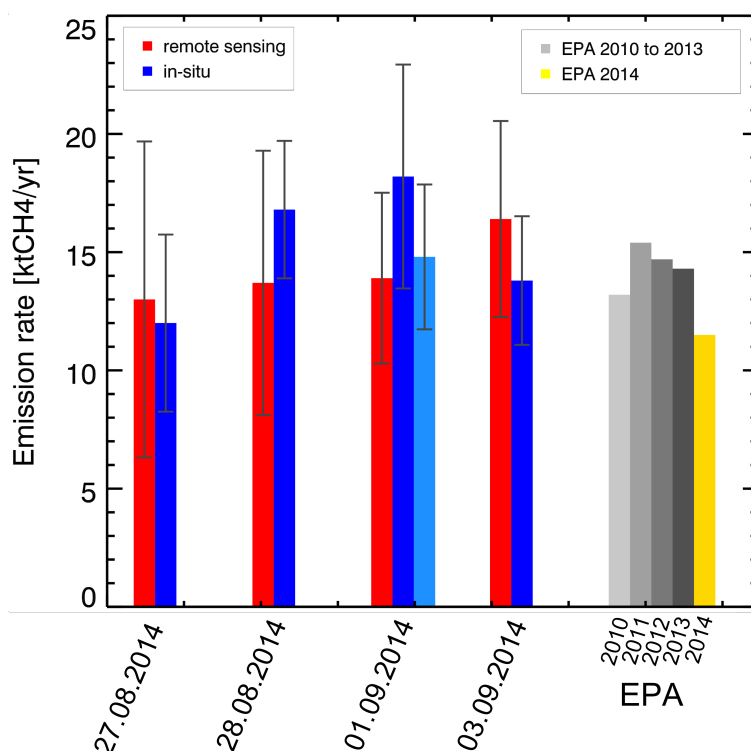


Figure 10. The bar charts show the derived emissions and inventory values. The first four sets of bars depict the derived emissions from this study based on the remote sensing (red), in-situ (blue; on the 01.09.2014: Dark blue: Downwind wall 1, bright blue: Downwind wall 2) measurements and their related errors (vertical bars). The fifth set shows the EPA inventory values for the years 2010 to 2013 (grey shaded) and 2014 (yellow).

7.2 Qualitative comparison between MAMAP and AVIRIS-NG data

On 03.09.2014, contemporaneous AVIRIS-NG measurements were performed and made available for a qualitative comparison. Figure 11 shows a comparison of the MAMAP remote sensing data on that day with one flight line acquired by AVIRIS-NG at around 13:33 local time. The MAMAP remote sensing measurements were acquired between 13:30 and 14:15 local time.

- To better visualize the CH_4 plume(s) detected by the AVIRIS-NG instrument on smaller scales, only measurements above a certain threshold are shown in the plot.

The AVIRIS-NG data shows a clear plume developing on the south-western slope of the landfill (red arrow) and travelling in downwind direction. It is in good agreement with the CH_4 plume seen by the MAMAP instrument.

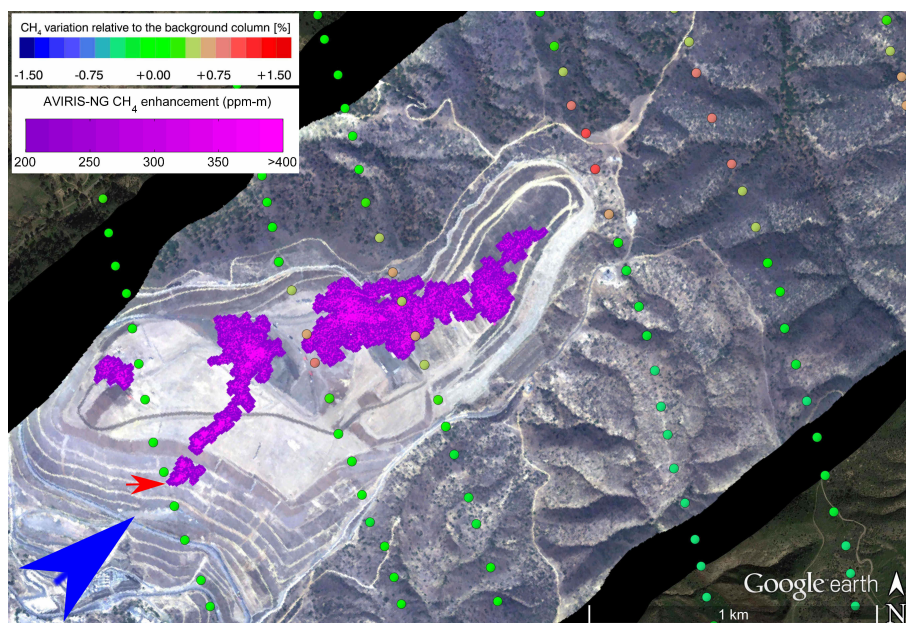


Figure 11. The MAMAP remote sensing (coloured circles) and the AVIRIS-NG (pink shaded areas) measurements on the 03.09.2014 are shown. The RGB map underneath is also based on AVIRIS-NG observations. For better source attribution, only AVIRIS-NG measurements having a methane column enhancement of larger than 200 ppm · m are shown. The non threshold filtered flight track is depicted in the Fig. 9. The blue arrow depicts the approximate wind direction. Map underneath is provided by Google Earth.

7.3 Comparisons with the EPA inventory

Compared to the EPA inventory value of 11.5 kt CH₄ for 2014, our estimated emission rates are on average around 3.0 kt CH₄ yr⁻¹ (with an uncertainty¹⁰ of ± 1.5 kt CH₄ yr⁻¹) larger. Due to the scatter of the estimated emission rates and the limited number of measurement days, it is not possible to conclude that EPA is significantly underestimating the Olinda Alpha Landfill CH₄ emissions. It is also important to note that the derived fluxes in this work, expressed in units of kt CH₄ yr⁻¹, are only snapshots and valid for the time of the overflight (here: in the afternoon). In addition, the difference could also arise from the possible leakage identified in the AVIRIS-NG observations, which is not taken into account by EPA, assuming that it was present on all measurement days. Furthermore, e.g., atmospheric pressure variations could potentially also lead to a deviation of the derived fluxes from the inventory value but are difficult to quantify.

8 Summary and conclusions

During the COMEX campaign, a comprehensive set of measurements over landfills located in the Los Angeles Basin has been collected. This study analyses in detail the airborne measurements over the Olinda Alpha Landfill. This landfill showed

¹⁰based on error propagation of the single flux uncertainties given in Table 2 and the statistical error



well-developed atmospheric CH₄ plume structures on all four measurements days conducted within on week in late summer 2014.

During this time period, measurements of column-averaged dry air mole fractions, XCH₄, were acquired by the MAMAP remote sensing instrument while flying above the atmospheric boundary layer. In addition, after each remote sensing survey, consecutive in-situ measurements of CH₄ and CO₂ and other atmospheric parameters like wind speed and wind direction were gathered while probing the atmospheric boundary layer and crossing the plume emitted by the landfill.

Using the collected data, the CH₄ emission rate of the landfill has been estimated from the remote sensing data and compared to the emission rate derived from the in-situ measurements. For that, an adapted mass balance approach has been used for the emission rate estimates from the remote sensing data. In order to interpret and analyse the in-situ measurements, a Kriging method has been applied. The average absolute difference between the estimates from both data sets is 2.3 kt CH₄ yr⁻¹ showing that the estimated emission rates agree well within the errors bars.

The resulting emissions have a range from around 13.0 to 18.2 kt CH₄ yr⁻¹ with case dependent relative uncertainties of around 17 % to 46 %. The contribution of the different error sources to the total uncertainty varies from case to case. For example, the remote sensing based emission rates are rather sensitive to the chosen background normalization area. Additionally, the uncertainty of the remote sensing based emission rates, which is caused by a not constant CO₂ background concentration or by co-emitted CO₂ from the landfill, has been estimated by utilizing the CH₄ and CO₂ in-situ measurements.

In terms of the in-situ measurements, concentration measurements of CH₄ at the surface would significantly lower the error in most cases. The error related to the Kriging method used for interpolation between the different flight legs has maximally the same size as other errors but is generally only a minor contributor to the budget whereas it is also based on conservative assumptions.

There is also a good agreement in plume position between the CH₄ column enhancements observed by the non-imaging MAMAP instrument and the imaging AVIRIS-NG instrument for data obtained on 03.09.2014. The AVIRIS-NG observations make it possible to identify a CH₄ emission hot spot at the slope of the landfill, which could be a potential leakage, e.g., a leak in the cover layer.

Compared to the EPA inventory value, our estimates are on average 3.0 kt CH₄ yr⁻¹ (± 1.5 kt CH₄ yr⁻¹) higher. This difference might be related to the identified potential leakage not considered by the EPA inventory value or by other reasons e.g., atmospheric pressure variations.

Our study shows for the first time, that medium resolution (Full Width at Half Maximum, FWHM ≈ 0.9 nm) airborne based remote sensing measurements in the SWIR region around 1.65 μm are well suited to estimate the total CH₄ emission from a large landfill.

Acknowledgements. The authors declare that they have no conflict of interest. Development of MAMAP was jointly funded by the University and State of Bremen and the Helmholtz Center Potsdam - GFZ German research Centre for Geosciences.

The MAMAP activities within the CO₂ and Methane EXperiment (COMEX) were funded in parts by the University and the State of Bremen, the European Space Agency (ESA) and the National Aeronautics and Space Administration (NASA).



We would like to thank NASA AMES for the support regarding campaign coordination. Especially, we would also like to thank the CIRPAS team for the support during the entire campaign.



References

- Amini, H. R., Reinhart, D. R., and Mackie, K. R.: Determination of first-order landfill gas modeling parameters and uncertainties, *Waste Management*, 32, 305 – 316, doi:http://dx.doi.org/10.1016/j.wasman.2011.09.021, 2012.
- Amini, H. R., Reinhart, D. R., and Niskanen, A.: Comparison of first-order-decay modeled and actual field measured municipal solid waste landfill methane data, *Waste Management*, 33, 2720 – 2728, doi:http://dx.doi.org/10.1016/j.wasman.2013.07.025, 2013.
- 5 Babilotte, A., Lagier, T., Fiani, E., and Taramini, V.: Fugitive Methane Emissions from Landfills: Field Comparison of Five Methods on a French Landfill, *Journal of Environmental Engineering*, 136, 777–784, doi:10.1061/(ASCE)EE.1943-7870.0000260, 2010.
- Bovensmann, H., Buchwitz, M., Burrows, J. P., Reuter, M., Krings, T., Gerilowski, K., Schneising, O., Heymann, J., Tretner, A., and Erzinger, J.: A remote sensing technique for global monitoring of power plant CO₂ emissions from space and related applications, *Atmospheric Measurement Techniques*, 3, 781–811, doi:10.5194/amt-3-781-2010, 2010.
- 10 Buchwitz, M., Rozanov, V. V., and Burrows, J. P.: A near-infrared optimized DOAS method for the fast global retrieval of atmospheric CH₄, CO, CO₂, H₂O, and N₂O total column amounts from SCIAMACHY Envisat-1 nadir radiances, *Journal of Geophysical Research: Atmospheres*, 105, 15 231–15 245, doi:10.1029/2000JD900191, 2000.
- Buchwitz, M., Reuter, M., Bovensmann, H., Pillai, D., Heymann, J., Schneising, O., Rozanov, V., Krings, T., Burrows, J. P., Boesch, H., Gerbig, C., Meijer, Y., and Löscher, A.: Carbon Monitoring Satellite (CarbonSat): assessment of atmospheric CO₂ and CH₄ retrieval errors by error parameterization, *Atmospheric Measurement Techniques*, 6, 3477–3500, doi:10.5194/amt-6-3477-2013, 2013.
- 15 Caers, J.: Modeling uncertainty in the earth sciences, Wiley, Hoboken, NJ [u.a.], 2011.
- Cambaliza, M. O. L., Shepson, P. B., Caulton, D. R., Stirn, B., Samarov, D., Gurney, K. R., Turnbull, J., Davis, K. J., Possolo, A., Karion, A., Sweeney, C., Moser, B., Hendricks, A., Lauvaux, T., Mays, K., Whetstone, J., Huang, J., Razlivanov, I., Miles, N. L., and Richardson, S. J.: Assessment of uncertainties of an aircraft-based mass balance approach for quantifying urban greenhouse gas emissions, *Atmospheric Chemistry and Physics*, 14, 9029–9050, doi:10.5194/acp-14-9029-2014, 2014.
- 20 Capaccioni, B., Caramiello, C., no, F. T., and Viscione, A.: Effects of a temporary HDPE cover on landfill gas emissions: Multiyear evaluation with the static chamber approach at an Italian landfill, *Waste Management*, 31, 956 – 965, doi:http://dx.doi.org/10.1016/j.wasman.2010.10.004, 2011.
- 25 Chen, Y., Sun-Mack, S., Arduini, R. F., and Minnis, P.: Clear-sky and surface narrowband albedo variations derived from VIRS and MODIS Data, in: CONFERENCE ON CLOUD PHYSICS, CD ROM EDITION, 5.6 Atmospheric radiation 12th, Conference, Atmospheric radiation, vol. 12, Atmospheric radiation, Boston, Mass., USA, 2006.
- Cressie, N.: Statistics for spatial data, Wiley series in probability and mathematical statistics: Applied probability and statistics, J. Wiley, https://books.google.de/books?id=4SdRAAAAMAAJ, 1993.
- 30 Crosson, E.: A cavity ring-down analyzer for measuring atmospheric levels of methane, carbon dioxide, and water vapor, *Applied Physics B*, 92, 403–408, doi:10.1007/s00340-008-3135-y, 2008.
- Czepiel, P., Shorter, J., Mosher, B., Allwine, E., McManus, J., Harriss, R., Kolb, C., and Lamb, B.: The influence of atmospheric pressure on landfill methane emissions, *Waste Management*, 23, 593 – 598, doi:http://dx.doi.org/10.1016/S0956-053X(03)00103-X, second Intercontinental Landfill Resarch Symposium, 2003.
- 35 Eklund, B., Anderson, E. P., Walker, B. L., and Burrows, D. B.: Characterization of Landfill Gas Composition at the Fresh Kills Municipal Solid-Waste Landfill, *Environmental Science & Technology*, 32, 2233–2237, doi:10.1021/es980004s, 1998.



- ESA: Report for Mission Selection: CarbonSat, ESA SP-133/1 (2 volume series), European Space Agency, Noordwijk, The Netherlands, 2015.
- Farrance, I. and Frenkel, R.: Uncertainty of Measurement: A Review of the Rules for Calculating Uncertainty Components through Functional Relationships, *The Clinical Biochemical Reviews*, 33, 49–75, 2012.
- 5 Frankenberg, C., Thorpe, A. K., Thompson, D. R., Hulley, G., Kort, E. A., Vance, N., Borchardt, J., Krings, T., Gerilowski, K., Sweeney, C., Conley, S., Bue, B. D., Aubrey, A. D., Hook, S., and Green, R. O.: Airborne methane remote measurements reveal heavy-tail flux distribution in Four Corners region, *Proceedings of the National Academy of Sciences*, 113, 9734–9739, doi:10.1073/pnas.1605617113, 2016.
- Gebert, J. and Groengroeft, A.: Passive landfill gas emission - Influence of atmospheric pressure and implications for the operation of
10 methane-oxidising biofilters, *Waste Management*, 26, 245 – 251, doi:http://dx.doi.org/10.1016/j.wasman.2005.01.022, 2006.
- Gerilowski, K., Tretner, A., Krings, T., Buchwitz, M., Bertagnolio, P. P., Belemzov, F., Erzinger, J., Burrows, J. P., and Bovensmann, H.: MAMAP - a new spectrometer system for column-averaged methane and carbon dioxide observations from aircraft: instrument description and performance analysis, *Atmospheric Measurement Techniques*, 4, 215–243, doi:10.5194/amt-4-215-2011, 2011.
- Gerilowski, K., Krautwurst, S., Koyler, R., Jonsson, H., Krings, T., Horstjann, M., Leifer, I., Schuettemeyer, D., Fladeland, M., Burrows,
15 J. P., Bovensmann, H., Buchwitz, M., Hartmann, J., Sachs, T., Erzinger, J., Burrows, J. P., and Bovensmann, H.: Remote sensing of large scale methane emission sources with the Methane Airborne MAPper (MAMAP) instrument over the Kern River and Kern Front Oil fields and validation through airborne in-situ measurements - Initial results from COMEX, in: *American Geophysical Union AGU*, https://agu.confex.com/data/handout/agu/fm14/Paper_21807_handout_1014_0.pdf, 2014.
- Green, R. O., Eastwood, M. L., Sarture, C. M., Chrien, T. G., Aronsson, M., Chippendale, B. J., Faust, J. A., Pavri, B. E., Chovit, C. J., Solis,
20 M., Olah, M. R., and Williams, O.: Imaging Spectroscopy and the Airborne Visible/Infrared Imaging Spectrometer (AVIRIS), *Remote Sensing of Environment*, 65, 227 – 248, doi:10.1016/s0034-4257(98)00064-9, 1998.
- Hamlin, L., Green, R. O., Mouroulis, P., Eastwood, M., Wilson, D., Dudik, M., and Paine, C.: Imaging spectrometer science measurements for Terrestrial Ecology: AVIRIS and new developments, in: *Aerospace Conference, 2011 IEEE*, pp. 1–7, doi:10.1109/AERO.2011.5747395, 2011.
- 25 Hörmann, C., Sihler, H., Bobrowski, N., Beirle, S., Penning de Vries, M., Platt, U., and Wagner, T.: Systematic investigation of bromine monoxide in volcanic plumes from space by using the GOME-2 instrument, *Atmospheric Chemistry and Physics*, 13, 4749–4781, doi:10.5194/acp-13-4749-2013, 2013.
- IPCC: 2006 IPCC Guidelines for National Greenhouse Gas Inventories, 2006.
- Isaaks, E. H. and Srivastava, R.: *Applied geostatistics*, Oxford Univ. Press, New York, NY [u.a.], 1989.
- 30 Journel, A. and Huijbregts, C.: *Mining geostatistics*, Academic P., <http://katalog.suub.uni-bremen.de/DB=1/LNG=DU/CMD?ACT=SRCHA&IKT=8000&TRM=17378616>, 1978.
- Kirschke, S., Bousquet, P., Ciais, P., Saunoy, M., Canadell, J., Dlugokencky, E., Bergamaschi, P., Bergmann, D., Blake, D., Bruhwiler, L., Cameron-Smith, P., Castaldi, S., Chevallier, F., Feng, L., Fraser, A., Heimann, M., Hodson, E., Houweling, S., Josse, B., Fraser, P., Krummel, P., Lamarque, J.-F., Langenfelds, R., Le Quere, C., Naik, V., O'Doherty, S., Palmer, P., Pison, I., Plummer, D., Poulter, B.,
35 Prinn, R., Rigby, M., Ringeval, B., Santini, M., Schmidt, M., Shindell, D., Simpson, I., Spahni, R., Steele, L., Strode, S., Sudo, K., Szopa, S., Van Der Werf, G., Voulgarakis, A., Van Weele, M., Weiss, R., Williams, J., and Zeng, G.: Three decades of global methane sources and sinks, *Nature Geoscience*, 6, 813–823, doi:10.1038/ngeo1955, 2013.



- Krige, D. G.: A Statistical Approach to Some Basic Mine Valuation Problems on the Witwatersrand, *Journal of the Chemical, Metallurgical and Mining Society of South Africa*, 52, 119–139, doi:10.2307/3006914, 1951.
- Krings, T., Gerilowski, K., Buchwitz, M., Reuter, M., Tretner, A., Erzinger, J., Heinze, D., Pflüger, U., Burrows, J. P., and Bovensmann, H.: MAMAP - a new spectrometer system for column-averaged methane and carbon dioxide observations from aircraft: retrieval algorithm and first inversions for point source emission rates, *Atmospheric Measurement Techniques*, 4, 1735–1758, doi:10.5194/amt-4-1735-2011, 2011.
- Krings, T., Gerilowski, K., Buchwitz, M., Hartmann, J., Sachs, T., Erzinger, J., Burrows, J. P., and Bovensmann, H.: Quantification of methane emission rates from coal mine ventilation shafts using airborne remote sensing data, *Atmospheric Measurement Techniques*, 6, 151–166, doi:10.5194/amt-6-151-2013, 2013.
- 10 Krings, T., Neininger, B., Gerilowski, K., Krautwurst, S., Buchwitz, M., Burrows, J. P., Lindemann, C., Ruhtz, T., Schüttemeyer, D., and Bovensmann, H.: Airborne remote sensing and in-situ measurements of atmospheric CO₂ to quantify point source emissions, *Atmospheric Measurement Techniques Discussions*, 2016, 1–30, doi:10.5194/amt-2016-362, 2016.
- Lavoie, T. N., Shepson, P. B., Cambaliza, M. O. L., Stirn, B. H., Karion, A., Sweeney, C., Yacovitch, T. I., Herndon, S. C., Lan, X., and Lyon, D.: Aircraft-Based Measurements of Point Source Methane Emissions in the Barnett Shale Basin, *Environmental Science & Technology*, 49, 7904–7913, doi:10.1021/acs.est.5b00410, 2015.
- 15 Lee, C. M., Cable, M. L., Hook, S. J., Green, R. O., Ustin, S. L., Mandl, D. J., and Middleton, E. M.: An introduction to the NASA Hyperspectral InfraRed Imager (HypIRI) mission and preparatory activities, *Remote Sensing of Environment*, 167, 6 – 19, doi:http://dx.doi.org/10.1016/j.rse.2015.06.012, 2015.
- Mays, K. L., Shepson, P. B., Stirn, B. H., Karion, A., Sweeney, C., and Gurney, K. R.: Aircraft-Based Measurements of the Carbon Footprint of Indianapolis, *Environmental Science & Technology*, 43, 7816–7823, doi:10.1021/es901326b, 2009.
- Myhre, G., Shindell, D., Breon, F.-M., Collins, W., Fuglestedt, J., Huang, J., Koch, D., Lamarque, J.-F., Lee, D., Mendoza, B., Nakajima, T., Robock, A., Stephens, G., Takemura, T., and Zhang, H.: Anthropogenic and Natural Radiative Forcing, book section 8, pp. 659–740, Cambridge University Press, Cambridge, United Kingdom and New York, NY, USA, doi:10.1017/CBO9781107415324.018, www.climatechange2013.org, 2013.
- 25 NSWMA: Modern landfills: A far cry from the past, National Solid Wastes Management Association, <https://books.google.de/books?id=u77ZNwAACAAJ>, 2006.
- Peischl, J., Ryerson, T. B., Brioude, J., Aikin, K. C., Andrews, A. E., Atlas, E., Blake, D., Daube, B. C., de Gouw, J. A., Dlugokencky, E., Frost, G. J., Gentner, D. R., Gilman, J. B., Goldstein, A. H., Harley, R. A., Holloway, J. S., Kofler, J., Kuster, W. C., Lang, P. M., Novelli, P. C., Santoni, G. W., Trainer, M., Wofsy, S. C., and Parrish, D. D.: Quantifying sources of methane using light alkanes in the Los Angeles basin, California, *Journal of Geophysical Research: Atmospheres*, 118, 4974–4990, doi:10.1002/jgrd.50413, 2013.
- 30 Poulsen, T. G. and Moldrup, P.: Evaluating effects of wind-induced pressure fluctuations on soil-atmosphere gas exchange at a landfill using stochastic modelling, *Waste Management & Research*, 24, 473–481, doi:10.1177/0734242X06066363, 2006.
- Poulsen, T. G., Christophersen, M., Moldrup, P., and Kjeldsen, P.: Relating landfill gas emissions to atmospheric pressure using numerical modelling and state-space analysis, *Waste Management & Research*, 21, 356–366, doi:10.1177/0734242X0302100408, 2003.
- 35 Rella, C.: Accurate Greenhouse Gas Measurement: in Humid Gas Streams Using the Picarro G1301 Carbon Dioxide / Methane / Water Vapour Gas Analyzer, Tech. rep., Picarro Inc., http://www.picarro.com/products_solutions/trace_gas_analyzers/co_co2_ch4_h2o, 2010.
- Rothman, L., Gordon, I., Babikov, Y., Barbe, A., Benner, D. C., Bernath, P., Birk, M., Bizzocchi, L., Boudon, V., Brown, L., Campargue, A., Chance, K., Cohen, E., Coudert, L., Devi, V., Drouin, B., Fayt, A., Flaud, J.-M., Gamache, R., Harrison, J., Hartmann, J.-M., Hill, C.,



- Hodges, J., Jacquemart, D., Jolly, A., Lamouroux, J., Roy, R. L., Li, G., Long, D., Lyulin, O., Mackie, C., Massie, S., Mikhailenko, S., Müller, H., Naumenko, O., Nikitin, A., Orphal, J., Perevalov, V., Perrin, A., Polovtseva, E., Richard, C., Smith, M., Starikova, E., Sung, K., Tashkun, S., Tennyson, J., Toon, G., Tyuterev, V., and Wagner, G.: The HITRAN2012 molecular spectroscopic database, *Journal of Quantitative Spectroscopy and Radiative Transfer*, 130, 4 – 50, doi:<http://dx.doi.org/10.1016/j.jqsrt.2013.07.002>, 2013.
- 5 Rozanov, V., Rozanov, A., Kokhanovsky, A., and Burrows, J.: Radiative transfer through terrestrial atmosphere and ocean: Software package SCIATRAN, *Journal of Quantitative Spectroscopy and Radiative Transfer*, 133, 13 – 71, doi:<http://dx.doi.org/10.1016/j.jqsrt.2013.07.004>, 2014.
- Thompson, D. R., Leifer, I., Bovensmann, H., Eastwood, M., Fladelland, M., Frankenberg, C., Gerilowski, K., Green, R. O., Krautwurst, S., Krings, T., Luna, B., and Thorpe, A. K.: Real-time remote detection and measurement for airborne imaging spectroscopy: a case study
10 with methane, *Atmospheric Measurement Techniques*, 8, 4383–4397, doi:10.5194/amt-8-4383-2015, 2015.
- Thompson, D. R., Thorpe, A. K., Frankenberg, C., Green, R. O., Duren, R., Guanter, L., Hollstein, A., Middleton, E., Ong, L., and Ungar, S.: Space-based remote imaging spectroscopy of the Aliso Canyon CH₄ superemitter, *Geophysical Research Letters*, 43, 6571–6578, doi:10.1002/2016GL069079, 2016.
- Trapani, D. D., Bella, G. D., and Viviani, G.: Uncontrolled methane emissions from a MSW landfill surface: Influence of landfill features
15 and side slopes, *Waste Management*, 33, 2108 – 2115, doi:<http://dx.doi.org/10.1016/j.wasman.2013.01.032>, 2013.
- Tratt, D. M., Buckland, K. N., Hall, J. L., Johnson, P. D., Keim, E. R., Leifer, I., Westberg, K., and Young, S. J.: Airborne visualization and quantification of discrete methane sources in the environment, *Remote Sensing of Environment*, 154, 74 – 88, doi:<http://dx.doi.org/10.1016/j.rse.2014.08.011>, 2014.
- Xu, L., Lin, X., Amen, J., Welding, K., and McDermitt, D.: Impact of changes in barometric pressure on landfill methane emission, *Global
20 Biogeochemical Cycles*, 28, 679–695, doi:10.1002/2013GB004571, 2014.
- Zien, A. W., Richter, A., Hilboll, A., Blechschmidt, A.-M., and Burrows, J. P.: Systematic analysis of tropospheric NO₂ long-range transport events detected in GOME-2 satellite data, *Atmospheric Chemistry and Physics*, 14, 7367–7396, doi:10.5194/acp-14-7367-2014, 2014.